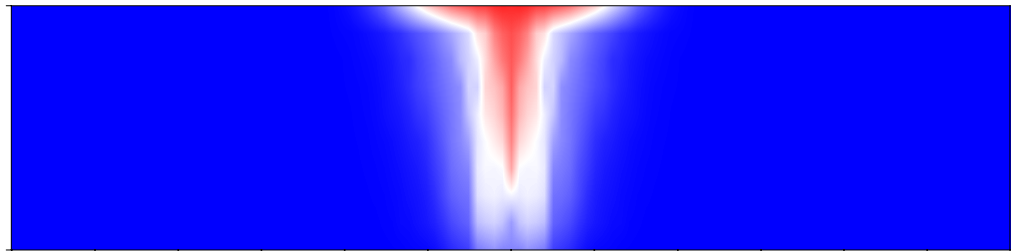


Saline Aquifer CO₂ Storage (SACS)

Final Report: Work Area 2 (Reservoir)



Profile of CO₂ plume after 2.5 years of injection in a homogenous formation



FINAL REPORT

Saline Aquifer CO₂ Storage (SACS): Task 2: Fluid and core properties and reservoir simulation.

Report period: 01/11/98 – 31/12/99

AUTHORS

Erik Lindeberg, SINTEF Petroleum Research
Bert van der Meer, NITG-TNO
Arild Moen, SINTEF Petroleum Research
Dag Wessel-Berg, SINTEF Petroleum Research
Amir Ghaderi, SINTEF Petroleum Research

CLASSIFICATION	ec-contract no.	CLIENTS	
Confidential	OG/306/98	EU Commission, BP Amoco, Norsk Hydro, Statoil, Vattenfall AB	
REG. NO.	DATE		
2000.025	28 April, 2000		
REPORT NO.		TASK CO-ORDINATOR AND EDITOR	SIGN.
54.5148.00/02/00		Erik Lindeberg	
NO. OF PAGES		LINE MANAGER	SIGN.
42		Torleif Holt	

SUMMARY

The over-all objective for this task is to predict the reservoir behaviour of CO₂ injected in the Utsira aquifer on short and long term in order to determine the quality of the reservoir as disposal for CO₂. The basis for this prediction is a model of the reservoir constructed on the basis of fluid and geophysical data as well as geological information obtained from seismics obtained prior to injection 1994, from cores and well logs. Fluid data and geophysical data have been obtained from literature data and laboratory studies under this task. The model will be calibrated by observation of time-lapse seismic. The first input of this from this seismic monitoring was obtained September 1999 after three years of injection.

The sensitivity of different reservoir parameters was determined by running several simulation tests. Within the range of reservoir and fluid parameters in the Utsira formation it was found that the most important geological data is cap rock topography for long term migration of CO₂. For short period of times (< 10 years) also the abundance, size and permeability of horizontal sales within the Utsira sand are important. A preliminary simulation model with impermeable shale layers has been constructed and tested on an injection scenario corresponding to the injection rates reported on well A16. The shales slow down the migration towards the top significantly compered to a homogenous case. Large amounts of CO₂ more or less temporally accumulates under the shales. A remarkable resemblance with the first seismic pictures after three years of injection was observed. This seismic picture provided the input for the first update of the model.

Table of Contents

1.	Introduction	4
2.	Thermodynamic data for the CO₂/CH₄/H₂O system.....	5
2.1	Experimental data	5
2.2	Thermodynamic conditions in offshore aquifers	6
2.2.1	Temperature gradient.....	6
2.2.2	Pressure gradient.....	7
2.3	Models for thermodynamic properties.....	7
2.3.1	Pure CO ₂	7
2.3.2	CO ₂ /methane mixtures.....	12
2.4	Application on Utsira temperature and pressure conditions	15
2.5	Solubility of CO ₂ in brine	16
2.6	Derivation of thermodynamic properties	17
2.7	Transport properties: Viscosity and diffusion.....	17
2.8	Conclusion	19
3.	Studies of cores in the Utsira formation.....	20
3.1	Core preparation.....	20
3.2	Porosity and permeability measurements	20
3.3	Capillary pressure and relative permeability	21
4.	Reservoir simulation	23
4.1	Selection of reservoir segment in Utsira and basic data and assumptions.....	23
4.2	Simulations on a homogeneous reservoir model	24
4.3	Heterogeneous reservoir model	27
4.4	Updating the reservoir model.....	28
4.5	Sensitivity with respect to permeability.....	29
4.6	Discussion of reservoir simulation.....	31
5.	Rayleigh convection.....	32
5.1	Summary	32
5.2	Defining equations	32
5.3	Derivation of pressure and concentration equation.....	34
5.3.1	Derivation of \vec{J}_p	35
5.4	Scaling of equations	36
5.4.1	Scaled constitutive relations	37
5.4.2	Scaled concentration equation	37
5.4.3	Scaled pressure equation.....	39
5.5	Perturbation analysis	39
5.6	Validation of perturbation analysis	40
6.	References	41

1. Introduction

CO₂ has been injected into the Utsira formation since September 1996. In the SACS project (Saline Aquifer CO₂ Storage) the basic objective is to monitor the migration of CO₂ in order to be able to determine the fate of CO₂ both on short time scale (< 50 years) and on a long time scale (1000's of years).

Simulation of CO₂ injection in aquifers can be simulated by most ordinary black-oil simulators as these can handle oil, gas and water phase and by simply leaving the oil out. Since typical black-oil simulators have a more sophisticated handling of the oil phase than the water phase, more flexibility can be achieved by rather leaving out the water phase and to give the oil phase the physical properties of water including CO₂/water phase properties (Lindeberg 1996). The input parameters for these simulators are mostly tabulated data. The formation volume factor and viscosity for respectively brine and CO₂ are the most important fluid parameters because they are the source for the buoyancy of CO₂ in the reservoir and the viscous drag of the fluid through the pores. Other important parameters are the pressure dependent solubility of gas in brine and capillary pressure. For simulation scenarios of less than 25 years the least important parameter is the molecular diffusion constant of CO₂ in brine, but this parameter can be important on long time scales when the final fate of CO₂ shall be predicted. There are of course several other parameters, which are important in simulation, but these parameters are related to the porous medium and are treated in a separate chapter. Permeability, porosity, capillary pressure and relative permeability including end-point saturations are important parameters on a microscopic scale and can be obtained from laboratory core experiments. For a reservoir scale simulation the most important input data for the reservoir grid is the distribution of heterogeneities and these must be obtained from seismic, well-logs of other geological input.

2. Thermodynamic data for the CO₂/CH₄/H₂O system

2.1 Experimental data

There exists a lot of experimental data from phase studies of CO₂. Much of this interest is due to its many industrial applications, e.g. as a solvent and extractant in process and food industry, as a coolant in the nuclear industry, as a refrigerant in the cooling machines and injectant in the petroleum industry. Many studies have been performed near the critical point not only because of its practical interest, but also because it is easy to create critical conditions in the laboratory (31°C, 73 bar). CO₂ is therefore particularly suited for studies of near-critical phenomena.

Many of the data obtained are measured at pressures and temperatures that are of less interest for the purpose of CO₂ disposal in aquifers, but there exist also many data in the regime (1 to 150 bar, 5 to 50 °C) which is of interest for this study. The most relevant data sets for this project are listed in Table 2.1.

Table 2.1 Selected measurement of CO₂ densities most relevant for this study

Authors	Year	Temp. °C	Pressure bar	Number of measurement
Michels <i>et al.</i>	1935	0 - 150	16 - 250	329
Kennedy	1954	0 – 1000	25 - 1400	2120
Vukalovich <i>et al.</i>	1968	0 – 750	1 – 600	493
Krillin <i>et al.</i>	1969	0 – 35	16 - 500	39
Reamer <i>et al.</i>	1944	38 - 238	14 – 700	142 (700)
Arai <i>et al.</i>	1971	-20 - 15	24 – 145	24 (181)

The CO₂ injected in Utsira is not pure CO₂, but contaminated with between 1 and 2.5% methane. This can have a pronounced effect on the density of the fluid especially near the saturation point. Experimental data for the CO₂/methane system is therefore also required. These are more scarce, but the two last references in Table 2.1 also include measurements for CO₂/methane mixtures (numbers in parentheses).

The injected CO₂ will also be saturated with water vapour. The partial pressure of water at these temperatures is so low that its contribution to total composition can be neglected. It will typically be below 0.07% of the total composition.

The solubility of CO₂ in water can, however, not be neglected especially when modelling the long-term fate of CO₂ in the aquifer. A lot of experimental data is available and most of the studies include experimental conditions that are relevant for the problems related to CO₂ disposal in aquifers.

2.2 Thermodynamic conditions in offshore aquifers

There exist a lot of thermodynamic models for CO₂ but many of these are valid or optimal in only limited temperature and pressure ranges. Some models, that can model near critical behaviour very well, may have large error at higher pressure and temperature and vice versa. Before a comprehensive test of various models it is therefore necessary to know what condition we shall simulate.

2.2.1 Temperature gradient

Heat is transported from the core of the earth to the surface due to primordial heat accumulated in the earth's history and heat generated by decay of radiogenic elements. The resulting temperature gradient in rock is controlled by this heat flow, the thickness of the crust, the conductivity of the rock, sediments and pore fluids and the surface temperature, in this case sea bottom temperature. Below 60 m the average sea bottom temperature is relatively constant over the region and is here set to 4.8°C. The conductivity of the rock varies laterally, and on a map reported by Eggen (1984) the gradient varies between 20 and 50 mK/m at various locations in the north Sea. The gradient can also vary vertically because the different sediments may have different conductance of heat, but in this study it is assumed that the gradient is linear between the sea floor and the formation. There exist only scattered temperature measurements at these depths and can at the present so the possibility to make a more advanced model is limited. There exist Utsira temperature measurements at the Grane, Oseberg and Sleipner locations and the resulting gradients are shown in Figure 2.1

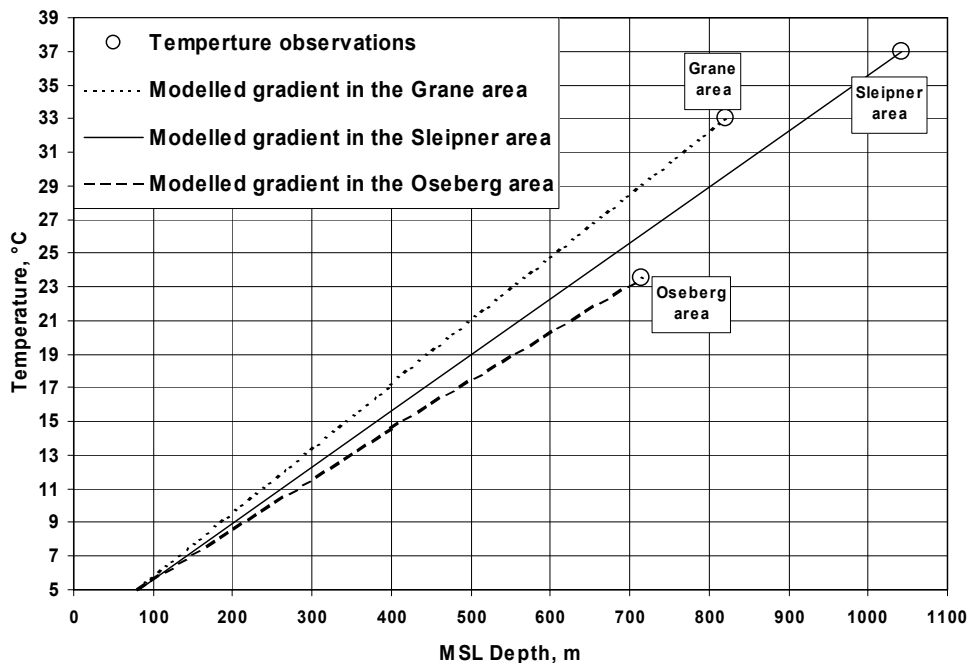


Figure 2.1 Temperature versus depth at three locations in the North Sea

The temperature gradient at low depth at Grane, Sleipner and Oseberg are respectively 29.2, 33.3 and 37.9 mK/m and are representative for the variations presented by Eggen

(1984). The recommended temperature profile between the sea floor at 80 m and the floor of the Utsira formation at (varying between 1100 to 1400 m) for this Utsira is accordingly

$$t = (z + 68) / 30 \quad (2.1)$$

where t is the temperature in °C and z is the depth in meter relative to mean sea level. (This is a significantly lower temperature gradient than the one estimated in the “Zero Task” pre-project).

2.2.2 Pressure gradient

In geological formation down to approximately 1500 m the pressure in the North Sea is typically controlled by the hydrostatic head. From the density profile of the brine the pressure profile can be calculated. The change in pressure with depth:

$$dp = \rho(p, t, c) g dz \quad (2.2)$$

where g is gravity constant, $\rho(p, t, c)$ is the density of brine as function of pressure, p , temperature, t , and concentration, c . The brine at these depths have a salinity and composition that can be compared to the sea water (3.5% salt). Because both the reservoir brine and the sea water brine has the same concentration it is assumed that the brine in column between the sea and the Utsira formation also has the same concentration. Experimental density of 3.5% brine has been taken from Engineering Science Data (1968) and the data set has been used to fit the density to a simple second order polynomial in p and t :

$$\rho = \sum_{j=0}^{j=2} \sum_{i=0}^{i=2} k_{ij} p^i t^j \quad (2.3)$$

and the function reproduces the data within 0.01% accuracy. Combining Equations 2.1, 2.2 and 2.3 eliminating either p or z gives a differential equation that is integrated from mean sea level to the sea floor at constant $t = 4.8$ °C to give the sea floor pressure. From the sea floor and down the equation is not separable (t is not constant) and the equation must be integrated numerically to give pressure as function of depth.

2.3 Models for thermodynamic properties.

2.3.1 Pure CO₂

In reservoir simulation simple cubic equation of states (EOS) are often used to provide the phase data for hydrocarbon mixtures. Some of these equations were therefor tested

on a set of experimental data at varying pressure at five different isotherms 25, 29, 32, 35 and 40°C. These were selected because they are relevant for the temperatures at various depth in a 700 to 1300 m deep aquifer. The cubic EOS that were investigated were the Soave-Redlich- Kwong (SRK) EOS and the Peng-Robinson (PR) EOS with and without the Peneloux translation volume correction. These four equations were compared with the experimental data of Michels and Krillin (Table 2.1). A fifth EOS that is included in this test it is a Lee-Kesler type EOS modified by Duan *et al.* (1992). This EOS has specifically been designed for the ternary system carbon dioxide /methane/ water and could therefore be a useful tool for the disposal problems since contamination of methane can be expected when the CO₂ source is not flue gas, but process waste from gas processing (*e.g.* Sleipner, Snøvit, Natuna). Also the other four EOS can handle mixtures. This equation was also used to model gas properties in a previous EU study (“Underground Carbon Dioxide Disposal”). Examples of the results are illustrated as deviation between measured and modelled densities for the isotherms 29.9°C, 32°C and 40°C in Figure 2.2 to Figure 2.4. The vertical grey line indicates the reservoir pressure for each isotherm in the Utsira formation.

The results show that in the gas phase the density prediction is relatively good for all EOS. The two Peng-Robinson EOS are the least accurate but with deviations less than 3%. In the dense phase, however, the four cubic EOS have significant deviation in the whole pressure range, but the error is particularly large near the Utsira conditions, up to 18%. The driving force for migration in the reservoir is not the density, but the buoyancy of CO₂ which is proportional to the density difference between brine and CO₂. The error in buoyancy is approximately 3 times larger than the error in density. The Lee-Kesler type EOS has also a significant deviation at low pressures, it performs relatively well. This trend is the same at all the five isotherms that were tested.

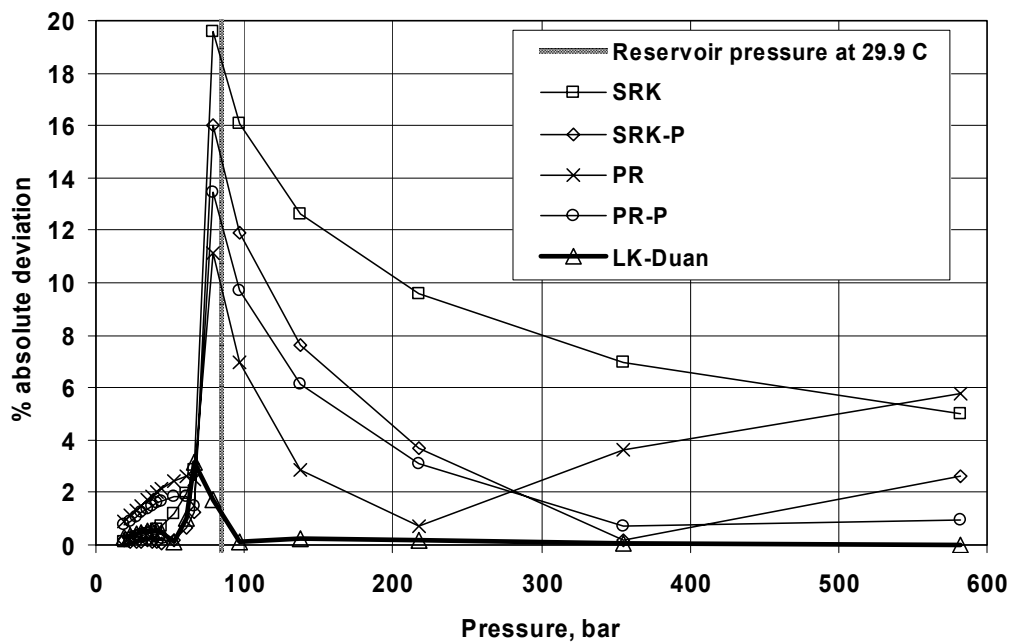


Figure 2.2 Deviation between calculated and measured CO₂ densities at 29.9°C. Four cubic and one Lee-Kesler EOS are tested (LK-Duan).

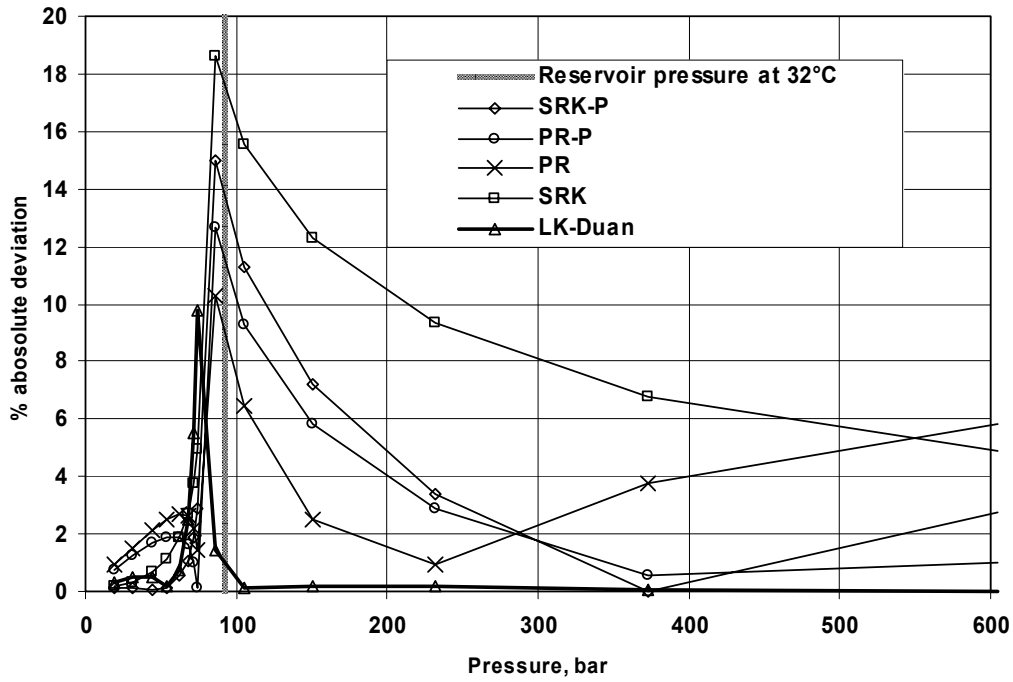


Figure 2.3 Deviation between calculated and measured CO_2 densities at $32^\circ C$. Four cubic and one Lee-Kesler EOS are tested. The Lee-Kesler EOS is modified by (Duan et al.).

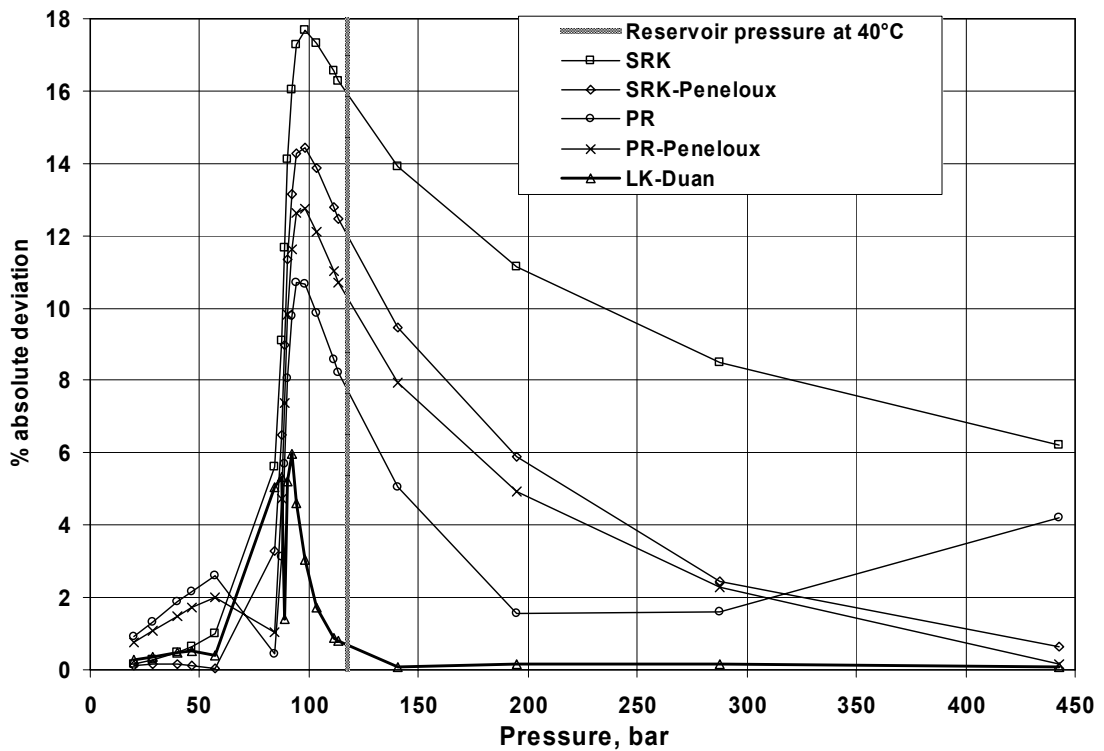


Figure 2.4 Deviation between calculated and measured CO_2 densities at $40^\circ C$. Four cubic and one Lee-Kesler EOS are tested. The Lee-Kesler EOS is modified by (Duan et al.).

The overall best of the four cubic EOS is the standard Peng-Robinson EOS and this should be selected if the choice is limited as it often is in compositional simulators. Simulation of CO₂ injection in aquifers can, however, be performed with black oil simulators where phase data are supplied as separate tabulated input. Then there is no limitation in the choice of EOS in the simulation. The more accurate, but also more complex LK EOS should then be preferred.

For pure CO₂ there also exist much more accurate EOS. The preferred EOS in IUPAC (1976) is a formulation by Altunin and Gadetskii (1971) which expresses the compression factor, Z , as

$$Z = 1 + \omega \sum_{i=0}^{i=9} \sum_{j=0}^{j=J_i} b_{ij} (\omega - 1)^i (\tau - 1)^j \quad (2.4)$$

where the inverse reduced temperature, $\tau = 394.2K / T$ and the reduced density, $\omega = \rho / 468$ where the density, ρ , is given in kg/m³. The b_{ij} 's are 50 disposable constants that has been obtained from approximately 1600 pVT data, saturation curve parameters and heat capacities. Near the critical point thermodynamic functions are non-analytic functions of ρ and T . An attempt to represent the critical point with an analytical equation will cause distortions which extend a considerable way into to the regions around it. Equation 2.4, which is not constrained at the critical point, will therefor not present an improved fit near the critical point compared to an equation that is constrained in the critical point. They will only fit differently in different regions. IUPAC has therefor recommended treating the near-critical region separately with a non-analytical approach and combining the two equations with a switching function. In this work it was found sufficient accurate to use the analytical part only as the maximum error is 0.78%.

The advantage of the LK EOS is that it contains a number disposable constants and these can be optimised for a more useful range than the data set used by Duan *et al.* They ambitiously optimised the pure component EOS for a temperature range of 0 to 1000°C and a pressure range of 0 to 8000 bar. For the ternary mixtures of CO₂/CH₄/H₂O, they reduced their ambitions to pressures up to 1000 bar. In this study the Duan *et al.*'s EOS has been modified by fitting it the data more representative for the problem related to underground and ocean disposal. In the following the resulting EOS fit is called the LK-SINTEF EOS.

In a second test the LK EOS in Duan version, in SINTEF version and the IUPAC EOS is compared for the same data set as above and the results are compared in Figure 2.5 and Figure 2.6 for two selected isotherms.

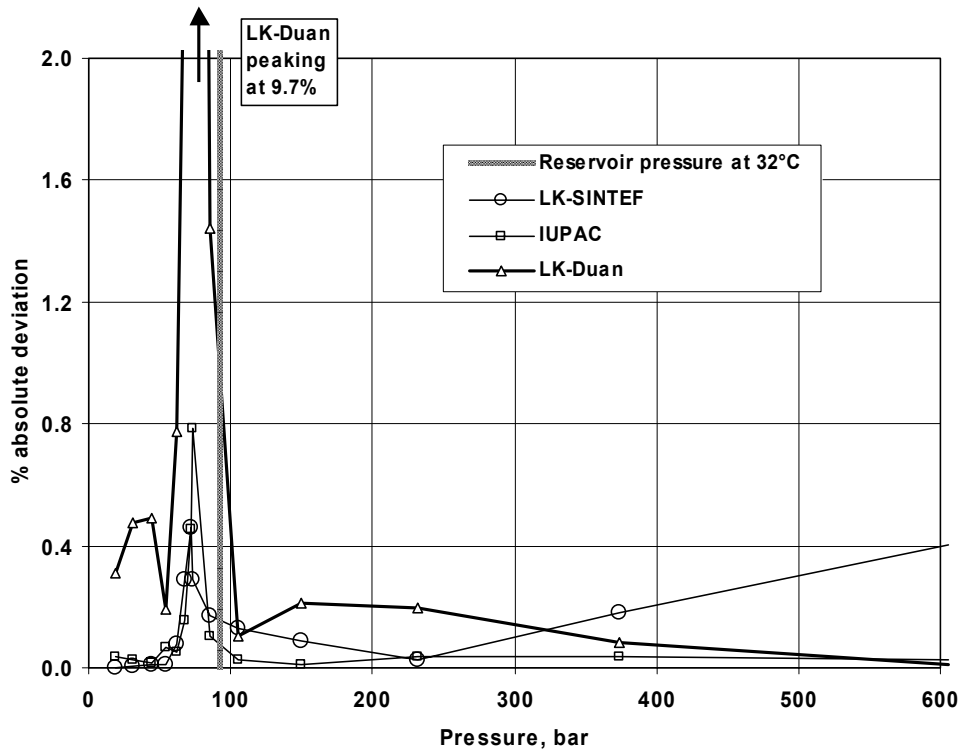


Figure 2.5 Deviation between calculated and measured CO₂ densities at 32°C. Two Lee-Kesler EOS and the analytical part of the IUPAC equation are compared in a test.

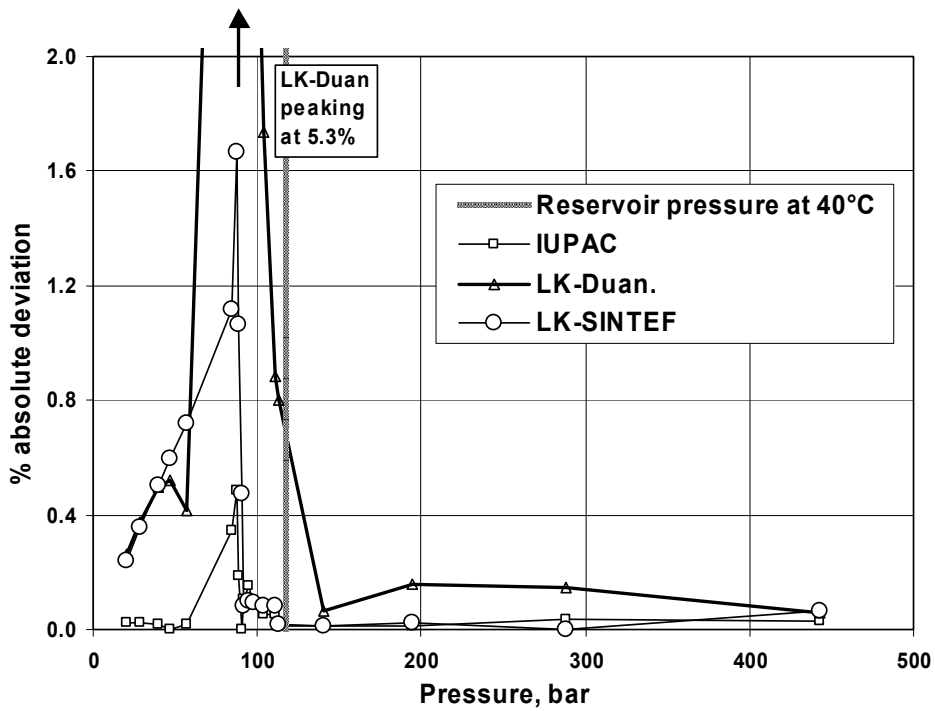


Figure 2.6 Deviation between calculated and measured CO₂ densities at 40°C. Two Lee-Kesler EOS and the analytical part of the IUPAC equation are compared in a test.

The results for all the seven EOS that were tested are summarised in Table 2.2.

Table 2.2 Test of seven different EOS on data for pure CO₂

Equation	Standard deviation in %	
	Whole data set 75 data points	Near geothermal/ hydrostatic gradient 10 data points
SRK	11.43	16.93
SRK-Peneloux	8.47	13.07
PR	5.80	8.50
PR-Peneloux	7.14	10.99
LK-Duan	3.82	1.14
LK-SINTEF	0.25	0.17
IUPAC (analytical part)	0.25	0.08

2.3.2 CO₂/methane mixtures.

When this report was written only a few measurements of methane concentration in the injected CO₂ were available. Nevertheless the reported values listed in Table 2.3, clearly indicate that the methane concentration is significant, and should be taken into account when the physical properties of the injectant are estimated.

Table 2.3 Reported methane concentrations in injection gas

Sampling date		Methane conc. in %
Sept. - Dec. 1996	(1.8 - 2.4%)	2.10
Feb. 22. 1997		2.08
Feb. 24. 1997		2.70
Feb. 25. 1997		2.37
"Average"		2.31

All the EOS above except the IUPAC equation can handle mixtures of CO₂ and methane. At the relatively low temperatures that are experienced in the Utsira formation, mixtures of CO₂ and methane are far from ideal, *i.e.* large excess will be seen. While pure CO₂ at Utsira conditions are not very close to the critical point, CO₂ with low content of methane can be much closer which is illustrated in Figure 2.7. Both these circumstances indicate that special attention should be exercised when the physical properties of these mixtures are modelled.

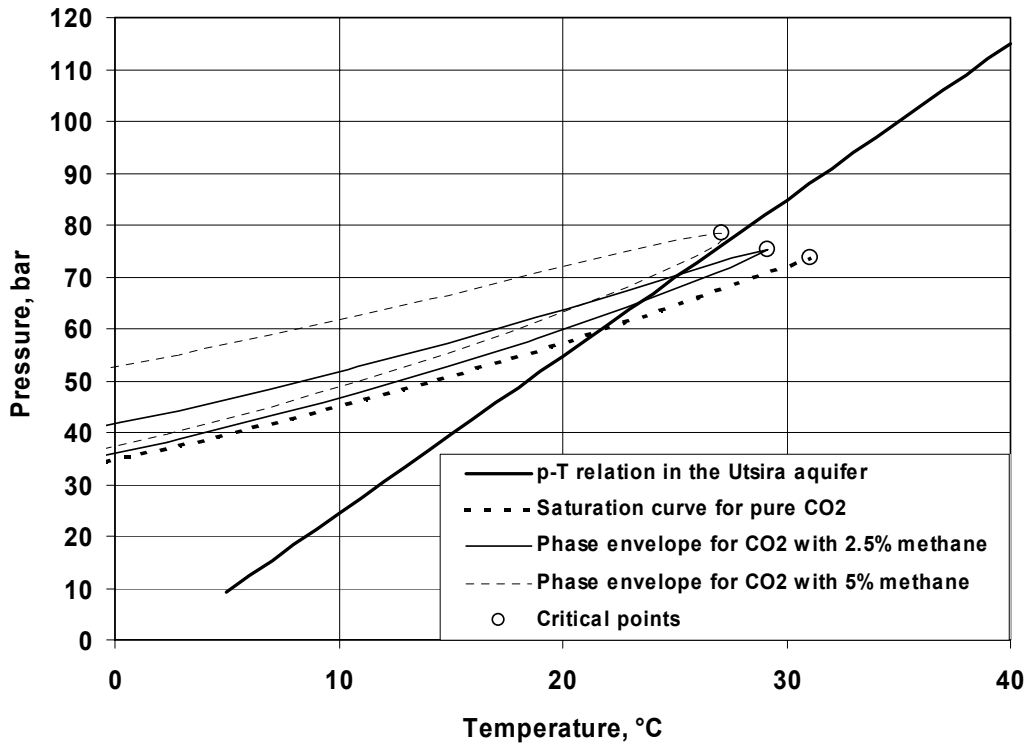


Figure 2.7 Phase envelopes for CO_2/CH_4 mixtures and the pressure-temperature relation in the Utsira formation.

Experimental data for CO_2 /methane mixtures are scarcer than for pure components. The two last references in Table 2.1 can however be used to fit models that are relevant for the pressure temperature regime of interest. The LK-Duan and the best of the cubic EOS that were tested for pure CO_2 above, are here compared with experimental excess volumes at an isotherm within the Utsira geothermal range. One example of the results is illustrated in Figure 2.8 for one temperature and pressure. This figure is corresponding to the density values illustrated in Figure 2.9.

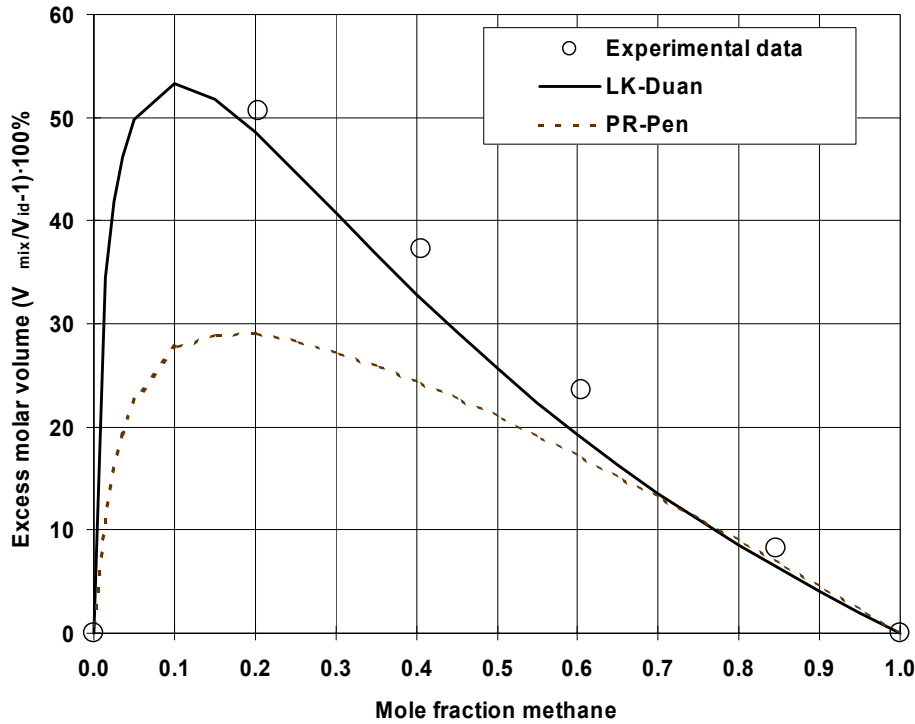


Figure 2.8 Experimental and modelled excess volumes for CO_2/CH_4 mixtures at 37.78°C and 86.2 bar. The experimental data point has been measured by Reamer et al. (1944)

The LK-Duan EOS has the disadvantage that it is discontinues at 31°C . If thermodynamic data are generated with the EOS for a continuous temperature gradient through the reservoir, a non-physical jump in the data will be experienced at 31°C .

This is due to that the three binary interaction coefficients, k_i , in the EOS are fitted to functions of temperature in two different ranges, one below 31°C and one above. In the following a modified version of LK-Duan equation is used. A switching function

$$s = (\tanh(K \cdot (t - t_m)) - 1) / 2 \quad (2.5)$$

has been introduced to achieve a smooth transition between the two ranges. In Equation (2.5) t is the temperature and t_m is the midpoint temperature for the function. The midpoint is chosen to 26.4°C because this is the arithmetic midpoint for the two closest available experimental isotherms (15°C respectively 37.8°C) with data for $\text{CO}_2/\text{methane}$. The constant, $K = 0.2$, determines how steep of the transition and is chosen to give the smoothest possible switching without changing the values of the binary interaction coefficient at the closest sets of data. The binary coefficient functions, $k_{i,lower}(t)$ and $k_{i,upper}(t)$ are combined in the following expression

$$k_i(t) = (1 - s) \cdot k_{i,lower}(t) + s \cdot k_{i,upper}(t) \quad i = 1, 2, 3 \quad (2.6)$$

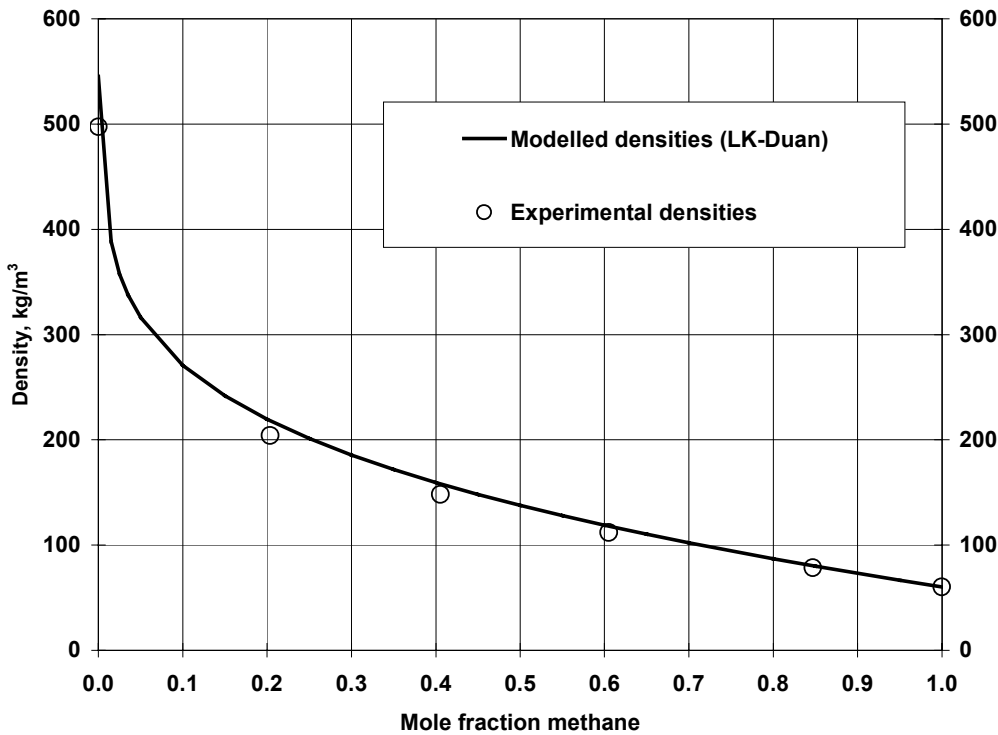


Figure 2.9 Experimental and modelled densities corresponding to the partial molar volumes illustrated in Figure 2.8

2.4 Application on Utsira temperature and pressure conditions

For a given temperature and pressure profile as function of depth it is now possible to model the density profile of CO₂. Using the simulated pressure and temperature profiles obtained in previous chapter as input, the CO₂ densities with varying amount of CO₂ is simulated of between sea floor at 80 m to the bottom of the formation at 1250 m depth was computed. The results are illustrated in Figure 2.10.

The most accurate profile is the curve for pure CO₂, but the densities of CO₂/methane mixtures are also sufficient accurate as input in reservoir simulation. The jump in the densities illustrate the depth where the state of CO₂ changes from dense (liquid) phase to gas. Above this depth the underground storage space is used much more inefficient. Previously (Holloway *et al.* 1996) estimated the minimum for storage depth has 800 meter based on a criterion of high-density requirement and simulation of Van der Sluijs (1991). The present simulation shows that this range could be extended to 530 m for pure CO₂ while CO₂ with 2.5% methane could be effectively stored in reservoirs with minimum depth of 680 meter (bold curve) if the CO₂ is injected offshore with a minimum water depth of 80 meter. At greater water depths CO₂ can be stored in dense phase in even in shallower formations. The difference in this results and previous estimates are most likely due to different surface temperature. Holloway *et al.* used average land temperature as lower temperature but here the offshore seafloor temperature is used This typically 5 to 10 °C lower than the average surface land

temperature in the boreal and temperate climate zones and this is significant also for the underground temperatures. Some of the difference can also be due to the CO₂ data, because it is not known what the basis is for the “Interactive thermodynamic data generator” used by Van der Sluijs.

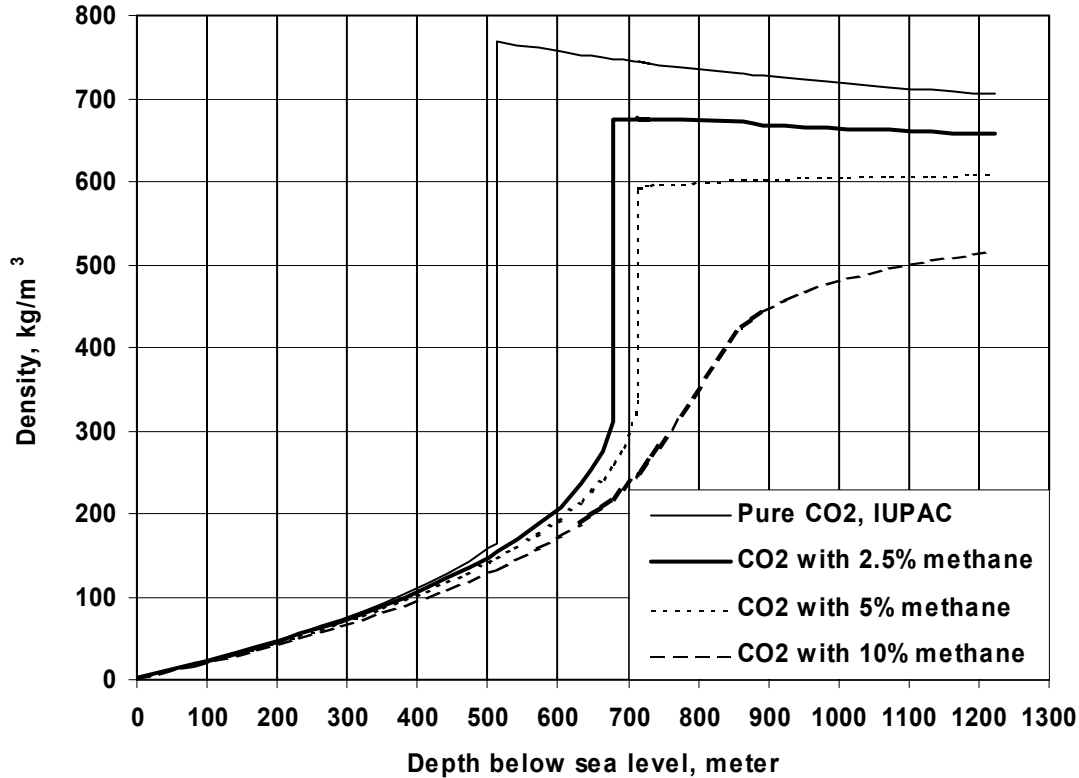


Figure 2.10 Density versus depth profiles of CO₂ and CO₂/methane mixtures at the pressure and temperature conditions in the Utsira formation

The simulations also provide a test for the switching function that was introduced in Equation 2.5. As seen from the density profiles, they are perfectly continuous at 31°C which is at approximately 870 m depth.

2.5 Solubility of CO₂ in brine

Solubility of CO₂ in brine is an important parameter for modelling the reservoir behaviour of CO₂, especially on long time scales. If the CO₂ during vertical migration has to pass through labyrinths of horizontal shales or other heterogeneities that can increase the amount of brine that is contacted by CO₂, solubility can play a significant role also on shorter time scales. On short time scale, however, great care must be exercised not to overestimate the solubility due to numerical dispersion. Application of fine gridding or up-scaling of the solubility are measures to reduce the effect of numerical dispersion.

One unit volume of brine can theoretically store approximately 10% of the one unit volume of pure CO₂ at reservoir conditions. Enick and Klara (1990) have reviewed a number of different models for CO₂ solubility in water and Krichevsky-Ilinskaya equations appears to be the most reliable. Solubility of CO₂ decreases with increased

concentration of brine and by combining the and Krichevsky-Ilinskaya equations with a method by Klins (1984) to correct for salt concentration in water, a complete model of CO₂ solubility in brine is achieved. Examples of the method are given in Figure 2.11 where the solubility at two isotherms is compared with experimental values. This model require accurate calculation partial molar volume of CO₂ in brine and the of fugacity of CO₂. The latter can be calculated from the EOS (ref. Paragraph 2.6)

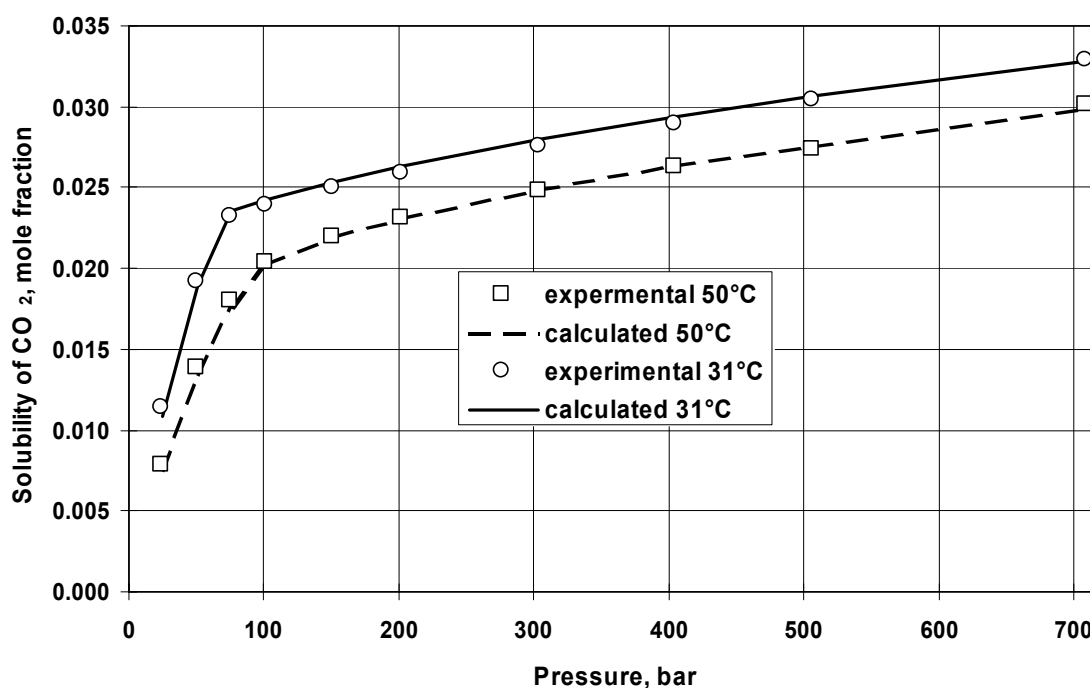


Figure 2.11 CO₂ solubilities modelled with Krichevsky-Ilinskaya equation compared to experimental values

2.6 Derivation of thermodynamic properties

Above only the density was tested for the different models. However, from the EOS all other thermodynamic properties like fugacity, entropy, enthalpy, internal energy, heat capacity and speed of sound can be calculating using standard thermodynamic method by mathematical manipulation of the EOS.

2.7 Transport properties: Diffusion and viscosity of in CO₂ and brine

Vukalovich (1968) has developed a model for the viscosity of CO₂. This model requires the density of CO₂ and the temperature as input. The model was tested on an experimental data set that has been obtained by Golubev (1959). A subset of the most relevant data was chosen and the results are shown in Figure 2.12. The standard deviation between modelled and experimental data for these 18 data is 3.9%.

In Figure 2.13 an application for the Utsira temperature and pressure conditions are applied.

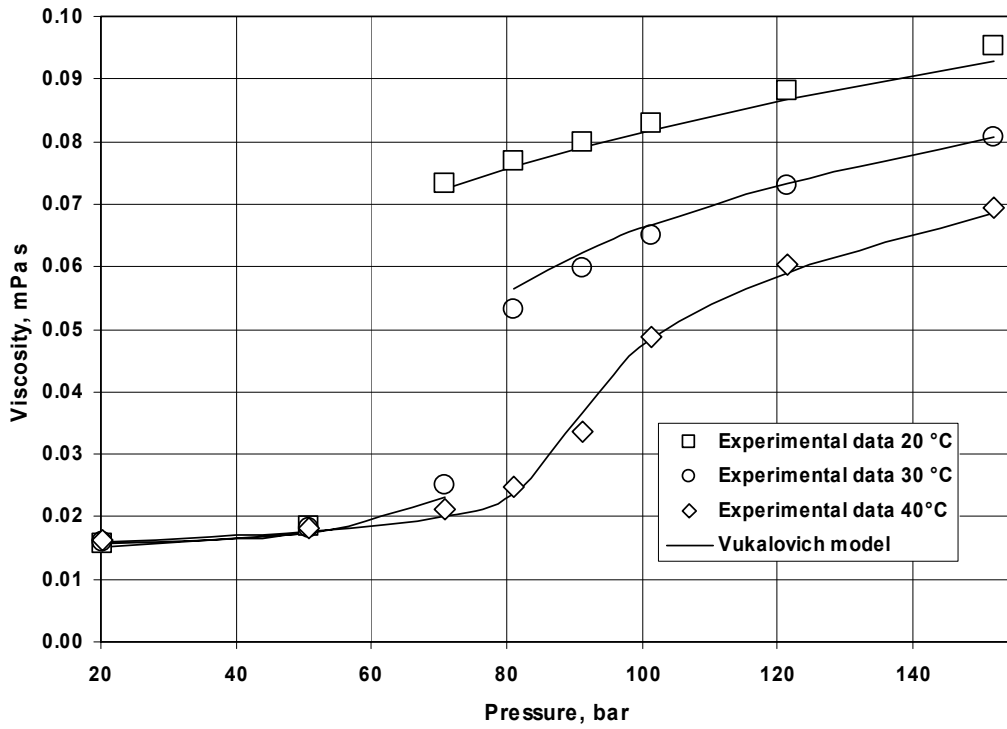


Figure 2.12 Experimental and modelled viscosities for CO₂. The data coincides for all three isotherms in the gas phase below 50 bar.

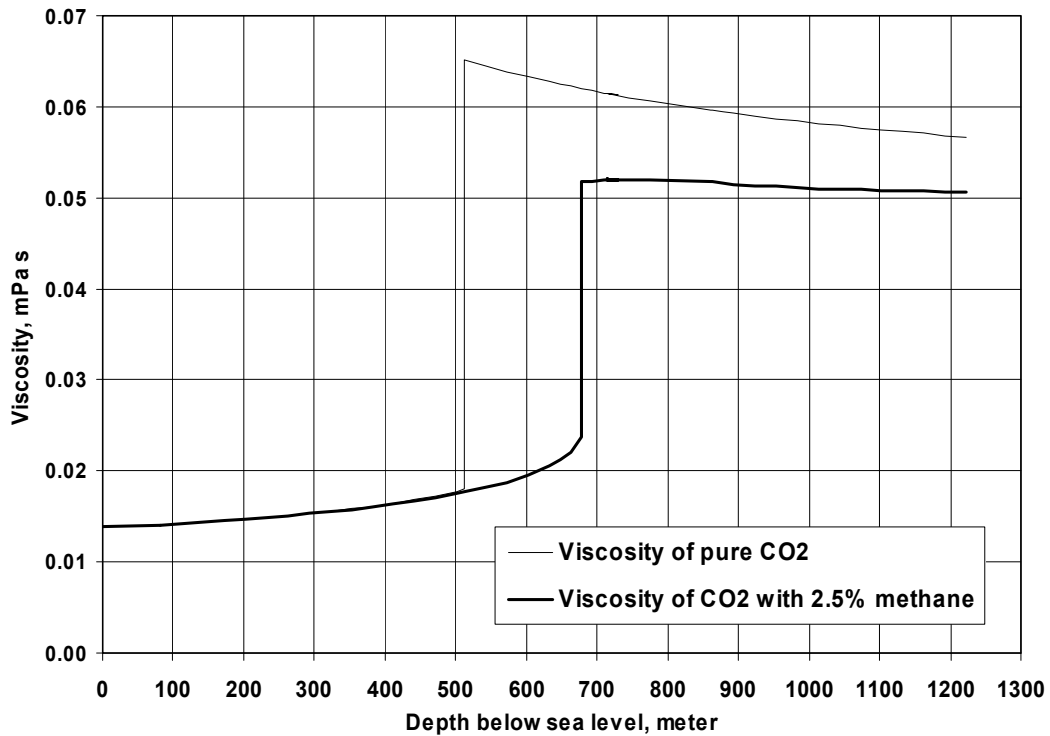


Figure 2.13 Simulated viscosity at reservoir conditions

Experimental viscosities for CO₂/methane mixtures have not been found and it remains to show how accurate the model of Vukalovich and Altunin is for mixtures with low methane concentration.

The method to determine viscosity of brine as function of temperature, pressure and salinity has been developed by Hewlett Packard and is reported in their “Petroleum Fluid Pack” which is a manual for a programme package. This method is based on a work by Numbere *et al.*(1977) and has been re-coded for use in this project.

Renner (1988) has correlated experimental diffusion coefficients for CO₂ in water to both his own high-pressure measurement and previously measured low-pressure data. It was shown that the diffusion coefficient, D_0 , correlated well to the gas and water viscosity, μ , by:

$$D_0 = 6391 \cdot \frac{\mu_{CO_2}^{6.911}}{\mu_{brine}^{0.1584}} \quad (2.7)$$

This correlation is based on measurements up to 59 bar at 37.8°C and extrapolation to into the dense-phase CO₂ region gives non-consistent results. The available reservoir simulators do, however, not use the diffusion constant data as function of pressure and temperature, so a single average value is sufficient. It is therefor recommended that the experimental value for the highest pressure measured by Renner is used for the entire depth. Considering the relative importance of diffusion compared to the other parameters in the simulation this should be sufficient.

2.8 Conclusion

For pure CO₂ there exists a wealth of experimental data at conditions which are interesting for underground CO₂ disposal. There exists also several equation of state that can model physical properties in for this purpose and the recommended model is the IUPAC EOS.

For CO₂/methane mixtures there are only a few data sets that are relevant for Utsira temperature and pressure conditions. Between 15 and 38°C there exists no data and there data for methane concentrations below 20% are scarce. It is recommended to obtain measurements for these conditions for further improving the LK-Duan EOS model, which is the most promising of the EOS tested for CO₂/methane mixtures.

3. Studies of cores in the Utsira formation

3.1 Core preparation

The cores were delivered as frozen samples in 4" aluminium tubes 1 meter long. Because the cores were totally unconsolidated, special care had to be observed to avoid unnecessary disturbance of the sand grains. Through some experimenting a recommended method was obtained.

The core sample contained so little formation water and was too loose for coring or cutting. The core was therefore carefully melted in its barrel, evacuated and then saturated with 3.5% brine. The core was then frozen again to -40°C in its barrel. In frozen condition the barrel was opened by milling two seams on each side and lifting of the two resulting half-pipes.

In this condition it was possible to take 1.5" cores for the remaining measurements.

3.2 Porosity and permeability measurements

The porosity was measured by both a helium porosimeter and when the evacuated core in a core holder 100 bar overburden pressure as sleeve pressure. The measurements were performed on different cores, but until more measurements exist, it is recommended to use the average value. The results are illustrated in Table 3.1.

Table 3.1 Porosity and permeability measurements

Sample	Method	Porosity, %	Permeability, Darcy
Utsira horizontal core 1	Water, lab	42.5	
Utsira vertical core	Helium, lab	35.0	3.25
Utsira horizontal core 2			2.55
Utsira core SINTEF average		38.8	2.90
Utsira core, other laboratory			~ 0.7
Utsira fm. Grane Area well	Well test	35	5.8
Utsira fm. Oseberg Area well	Well test	33 - 43	1.10 – 8.14

The permeability was measured on a 10 cm x 1.5" cores, mounted in a core holder with 100 bar sleeve pressure. The pressure drop across the core was recorded as function of water flow rate. The results are illustrated in Figure 3.1 and they are also tabulated in Table 3.1. The laboratory measurements show a surprisingly large variation considering that the core samples are taken from similar unconsolidated core material. This question must be carefully evaluated in future studies. The variation in the well test data are not so surprising due to the shales that have been observed on the well-logs.

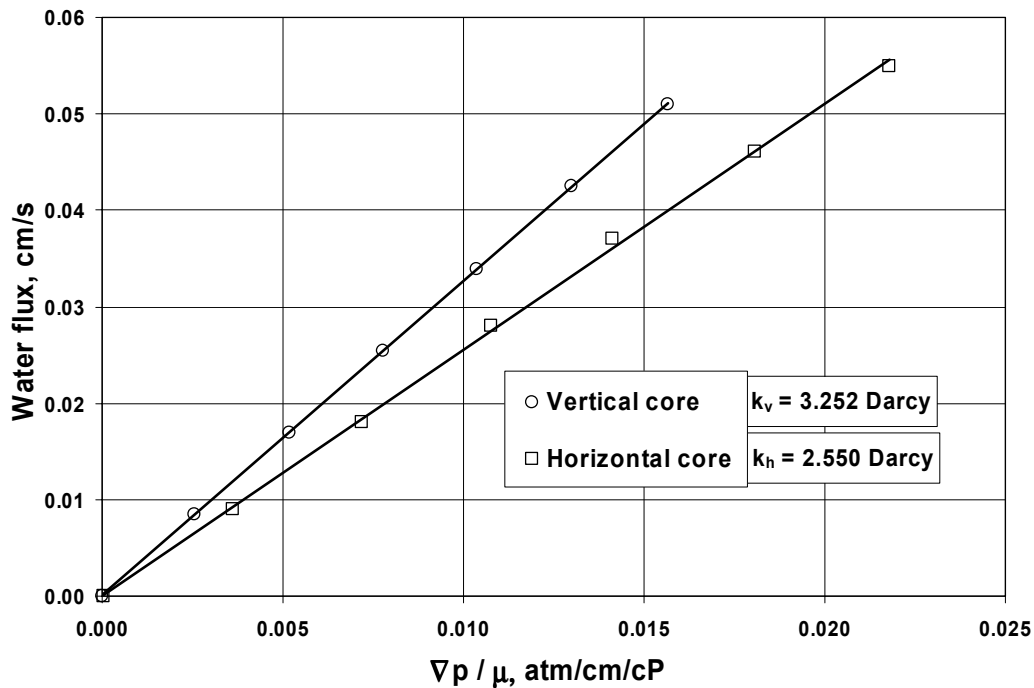


Figure 3.1 Flux versus pressure drop in permeability measurement on Utsira cores. The inclination represents the permeability

3.3 Capillary pressure and relative permeability

Capillary pressures were measured at ambient conditions in an ultra centrifuge. The core was originally saturated with brine and the production of brine was recorded as function of increased centrifugal acceleration. From the production data the corresponding air/brine capillary curve could be computed. This curve was reprocessed by help of air/brine and CO₂/brine interfacial tension data form Hough et al. (1959) and Eggers and Jäger (1994). The consistency of the two data sets (Figure 3.3) is questionable, but little relevant published data are available. Their data were obtained with pure water and not with brine. The final CO₂/brine capillary pressure curve is illustrated in Figure 3.2. No further work on relative permeability in Utsira cores has been completed so far in this project. Until better analysis exists, it is recommended to use the gas-brine relative permeability data for high permeable sandstone of Holt *et al.* (1995).

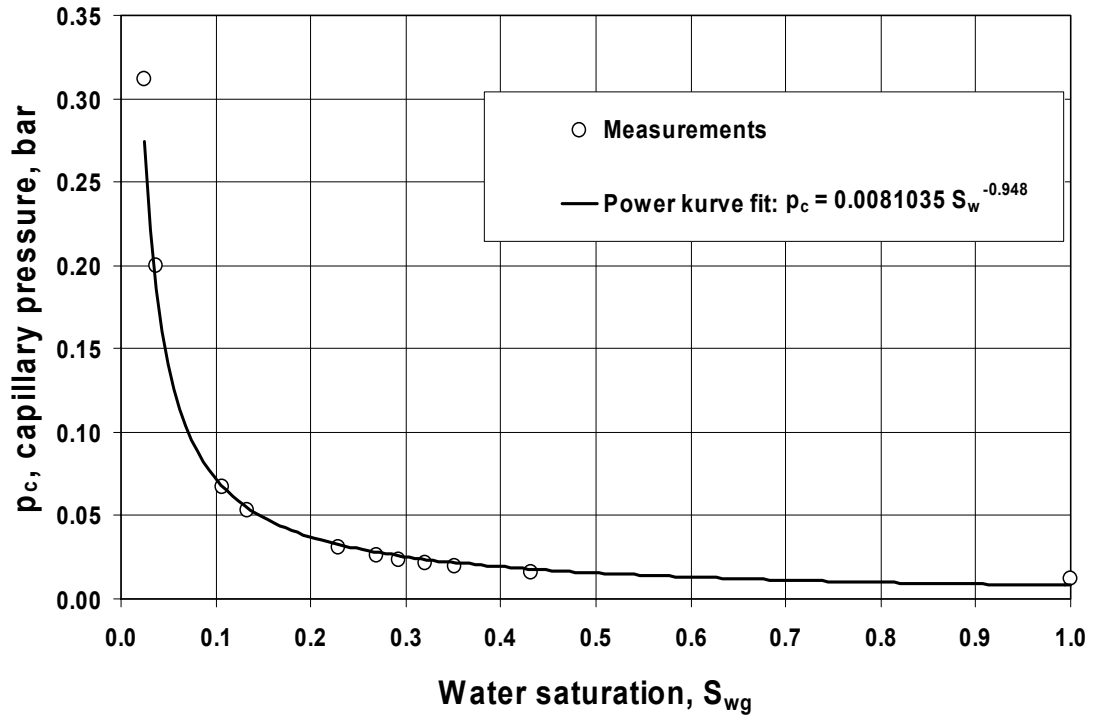


Figure 3.2 Capillary pressure curve obtained by ultracentrifuge measurements

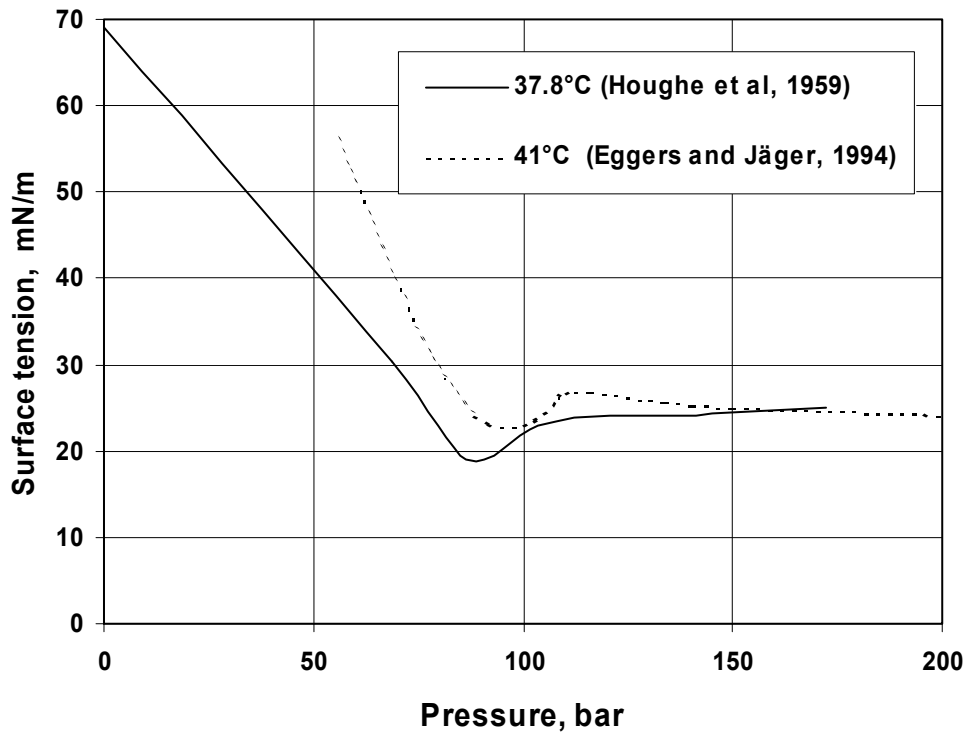


Figure 3.3 Surface tension between CO₂ and water at two different isotherms.

4. Reservoir simulation

Previous simulation of CO₂ injection into aquifers (Korbøll and Kaddour 1995, Lindeberg 1997) has shown that CO₂ readily will migrate to the sealing cap due to gravitational forces. A specific simulation on how fast this accumulation will occur is the objective for this part of the study.

4.1 Selection of reservoir segment in Utsira and basic data and assumptions.

From the supplied map of the Utsira top, Figure 4.1, a shallow anticline trap can be identified above the injection point. A simplified reservoir model has been built on the basis of a cylinder with 1600 m diameter below the circle shown on the figure. The actual model consists only of a 60° sector of this cylinder assuming an idealised radial geometry. In all cases the cap rock dip and extension from centre to spill point is kept constant (12.5 m dip on an 800 m radius). The real injection point is actually 300 m off the centre of the anticline, but for this simplified approach it has been placed in the centre at 960 m depth below sea mean level (add 78 m to achieve the true vertical depth relative to the rotary table on the Sleipner A platform). Initial hydrostatic pressure is applied and this pressure is maintained at the bottom of the periphery of the model corresponding to a situation with infinite extension of the whole formation. The injection well is horizontal, and the perforation is 40 m of which only 20 m will reach into the 60° sector, which is studied. The simulation is carried out with Eclipse 100 according to the method, fluid and relative permeability data used by Lindeberg (1996). The permeability used was 3.3 Darcy ($\sim 3.3 \cdot 10^{-12} \text{ m}^2$) in both vertical and horizontal direction. The numerical grid consists of up to 56 000 radial grid blocks. Molecular diffusion was not included during this simulation, while capillary pressure and solubility of CO₂ in brine were accounted for.

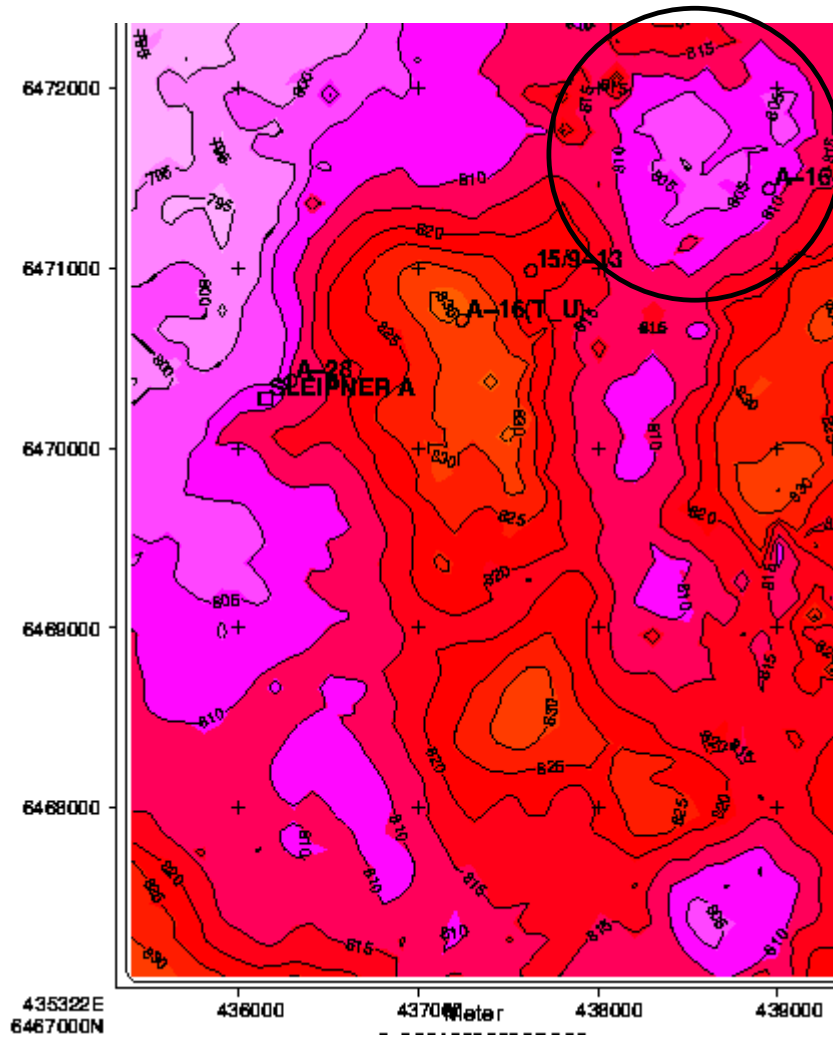


Figure 4.1 A map of the Utsira cap with the selected segment used in simulations indicated with a circle. The circle diameter is 1600 m.

4.2 Simulations on a homogeneous reservoir model

In this case it assumed that the reservoir is both a homogenous and isotropic body with a permeability of approximately 3.3 Darcy. Injection is simulated from start September 15th 1996. The CO₂ will migrate from the injection point to the cap seal in approximately three weeks. The CO₂ bubble will then gradually increase in radius until it reaches the spill point at December 1st. 1998 at 800 m radius. The CO₂ will then start to migrate to one of the three traps north, west or south of the injection trap (only the west and south traps are shown on the map cut out illustrated in Figure 4.2). The maximum thickness of the CO₂ gas cap at start August 15th 1999 is 20 m (Figure 4.2). 12.5 m of this is due to the topography of the seal, while 7.5 m is a down-dip cone in the proximity to where CO₂ ascending from the injection well reaches the gas cap.

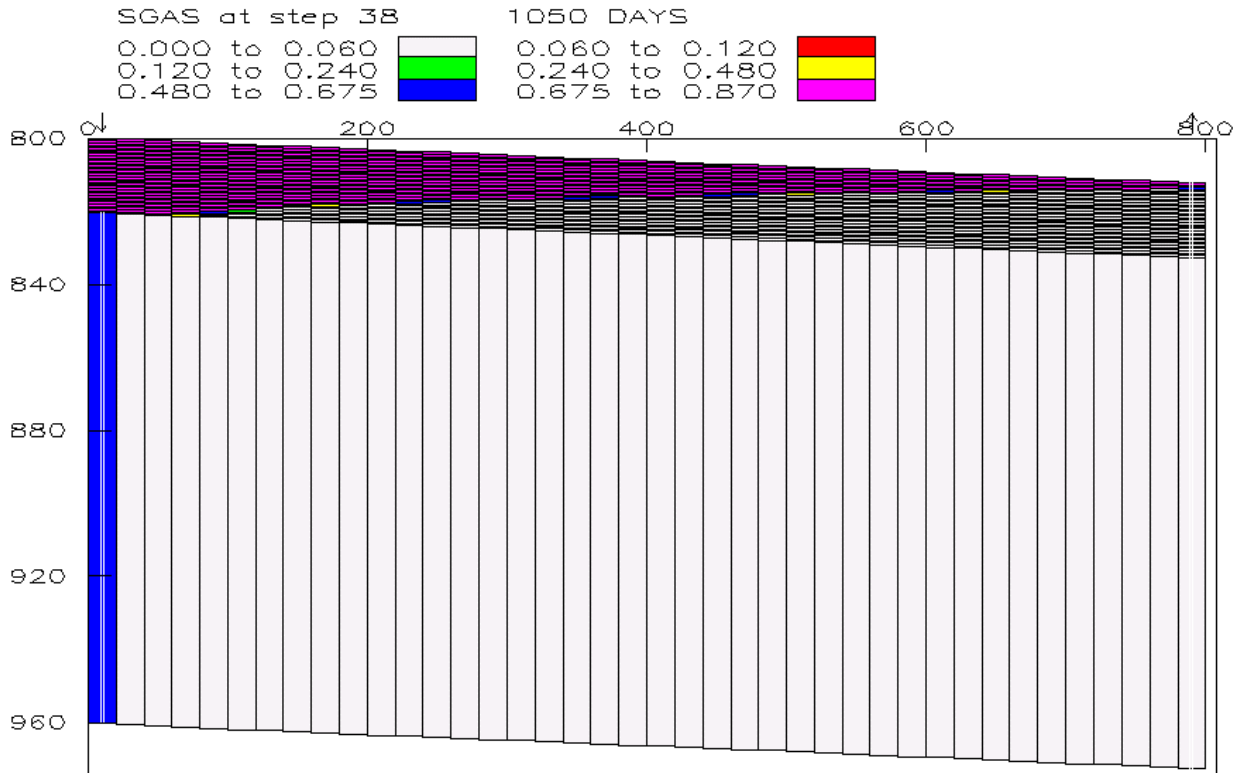


Figure 4.2 A vertical CO₂ saturation profile of the homogeneous reservoir model after 35 months of injection corresponding to the August 15th 1999. The CO₂ is injected in the lower left corner of the grid. Dimensions are in meters. The CO₂ has accumulated as a bubble in the anticline under the cap rock. The gas cap has not grown significantly since December 1st 1998 when the spill point was reached.

An alternative approach on a regional scale, the CO₂ distribution under a perfectly flat cap rock was simulated with a streamline simulator. The solubility of CO₂ is neglected, but this is not a big error when only short time intervals are considered. The advantage with this method is that numerical dispersion due block size is avoided. A result of these runs it was found that in a worse case scenario the CO₂ bubble would extent over a distance of 3000 meter from the injection point with an average thickness of 25 meter after an injection period of 20 years. For all these runs the injection rate was set at 1 million tonne CO₂ per year. Only small reservoir pressure increments were observed during these runs, this mainly due to the large extent of the Utsira formation (infinite aquifer) and the relative high permeability levels.

For fluid simulation on reservoir scale a downscaled version of the model above was used. The historical injection data has been converted to simulator input data. For the following simulation runs a uniform permeability of 3500 mD has been used. The calculated results are shown in the Figure 4.3 and Figure 4.4

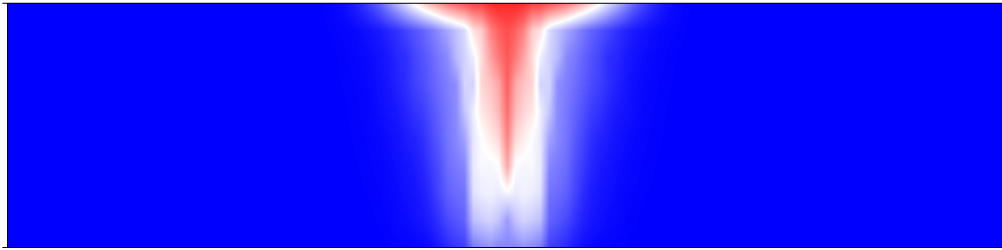


Figure 4.3 CO₂ Saturation cross section map at end of History Match period (861 days)

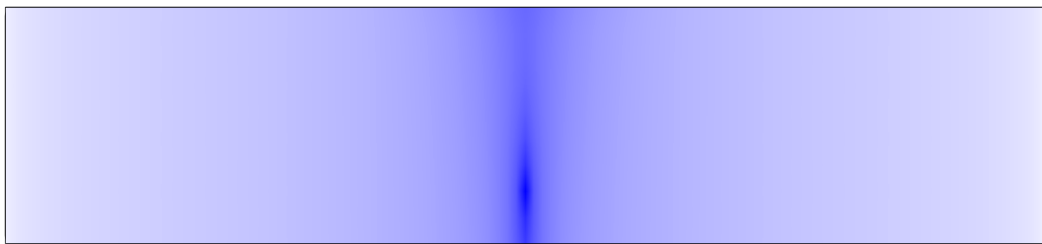


Figure 4.4 Pressure cross section map at end of History Match period (861 days)

The saturation map is showing a for CO₂ familiar picture, of a rising CO₂ column and CO₂ spreading pattern under the caprock. The horizontal CO₂ movement is mainly dictated by the relative large permeability. The pressure distribution is showing only small increments around, and directly above, the injection point

4.3 Heterogeneous reservoir model

In the heterogeneous reservoir model five impermeable layers of 400 m length have been distributed around the injection point corresponding to thin shale layers in a grid consisting of 10 000 blocks (250 x 40 blocks with size 1 m x 20 m). This is illustrated in transmissibility plot in Figure 4.5. The impermeable layers are visible as dark lines in the figure. The impermeable layers are supposed to resemble possible heterogeneities seen on well logs from the Utsira formation in the Sleipner area. The transport properties of these shales are not known, but they are assumed to perfectly impermeable in this model in order to introduce an extreme perturbation in flow the pattern of ascending CO₂.

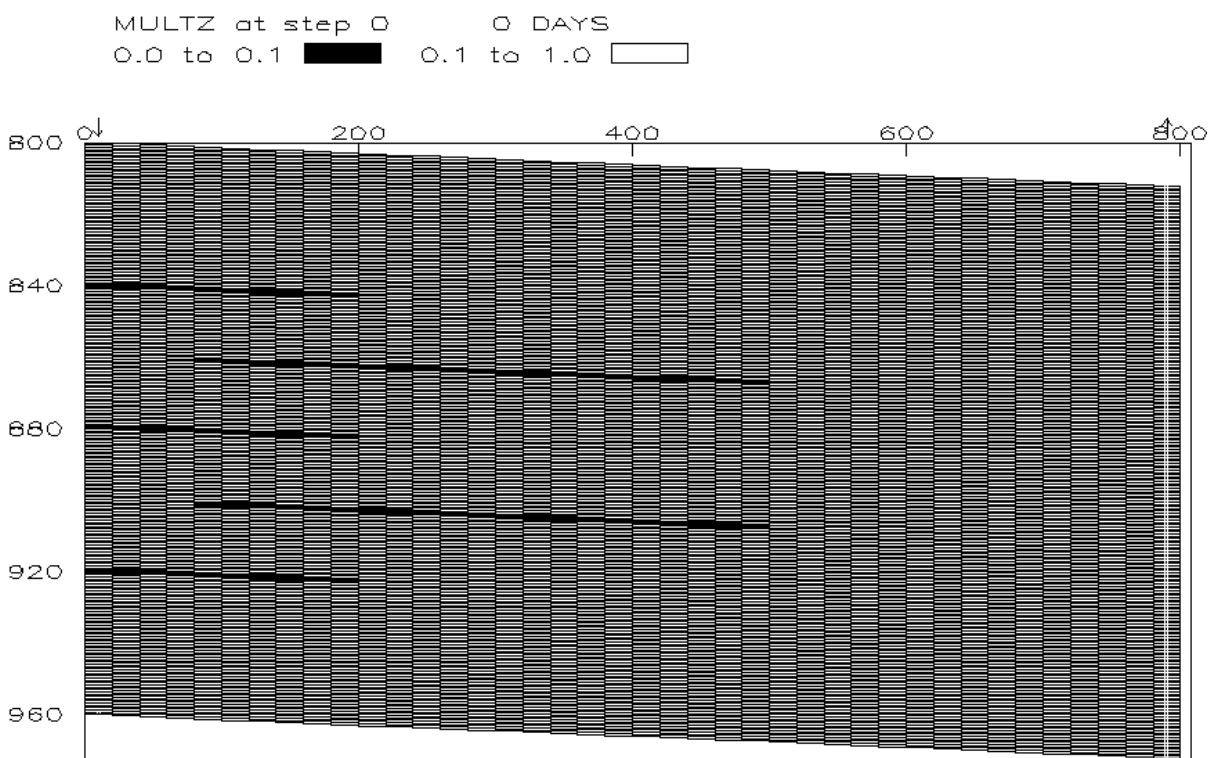


Figure 4.5 Transmissibility profile of the heterogeneous reservoir model. Illustration of the three anticline and two monocline impermeable layers introduced in the heterogeneous model. Only half of the central layers are seen in this reservoir cut-out due to symmetry.

The saturation profile after 35 months of injection is illustrated in Figure 4.6. Although the CO₂ has just recently reached the cap seal, there are large accumulations of CO₂ under the deeper impermeable layers. These bubbles has a thickness of up to 12 m and should also be detectable by seismic.

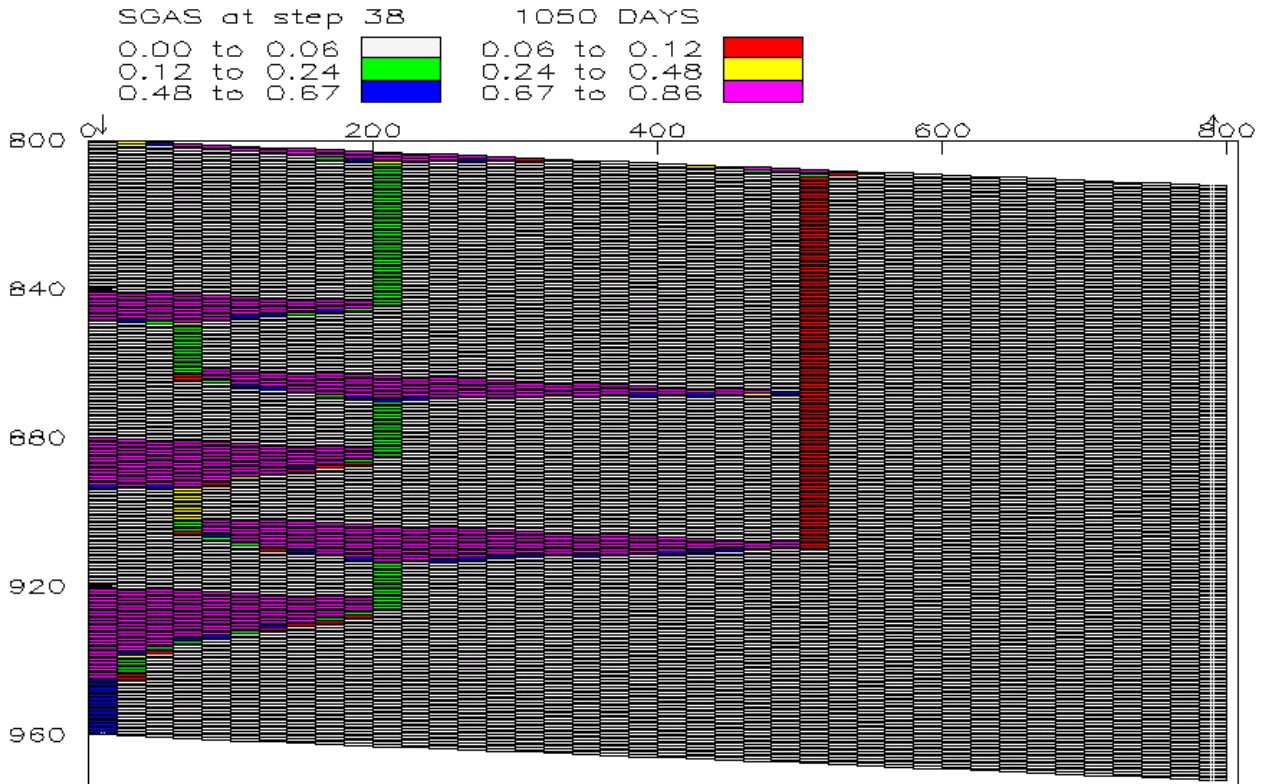


Figure 4.6 Saturation profile of the heterogeneous reservoir model after 35 month of injection (August 15th 1999). The CO₂ has recently reached the cap seal but large CO₂ bubbles have accumulated under impermeable shales.

4.4 Updating the reservoir model

The first possibility to update the model was when the first seismic results were obtained from the seismic survey after 3 years of injection. The result for this first seismic line is shown in Figure 4.7 and shows a remarkable resemblance to the results from simulations of the heterogeneous reservoir model. The preliminary interpretations can be performed:

1. CO₂ has reached the top Utsira as predicted from the simulations
2. Large amount of CO₂ is retained by layers parallel to the top similar to simulations.
3. The typical length of the deeper accumulation is approximately 500 m, while in the simulation they were 400 m.
4. The spacing between the layers is larger than in the preliminary model and accordingly not so many visible layers are present.
5. As also shown in the simulation will the anticline nearest to the injection point be filled relatively slowly due to the retention of large amount of CO₂ under deeper shales.
6. With this first seismic line there is not yet sufficient data to justify a larger or more refined model than what can be described in the symmetrical radial reservoir grid.

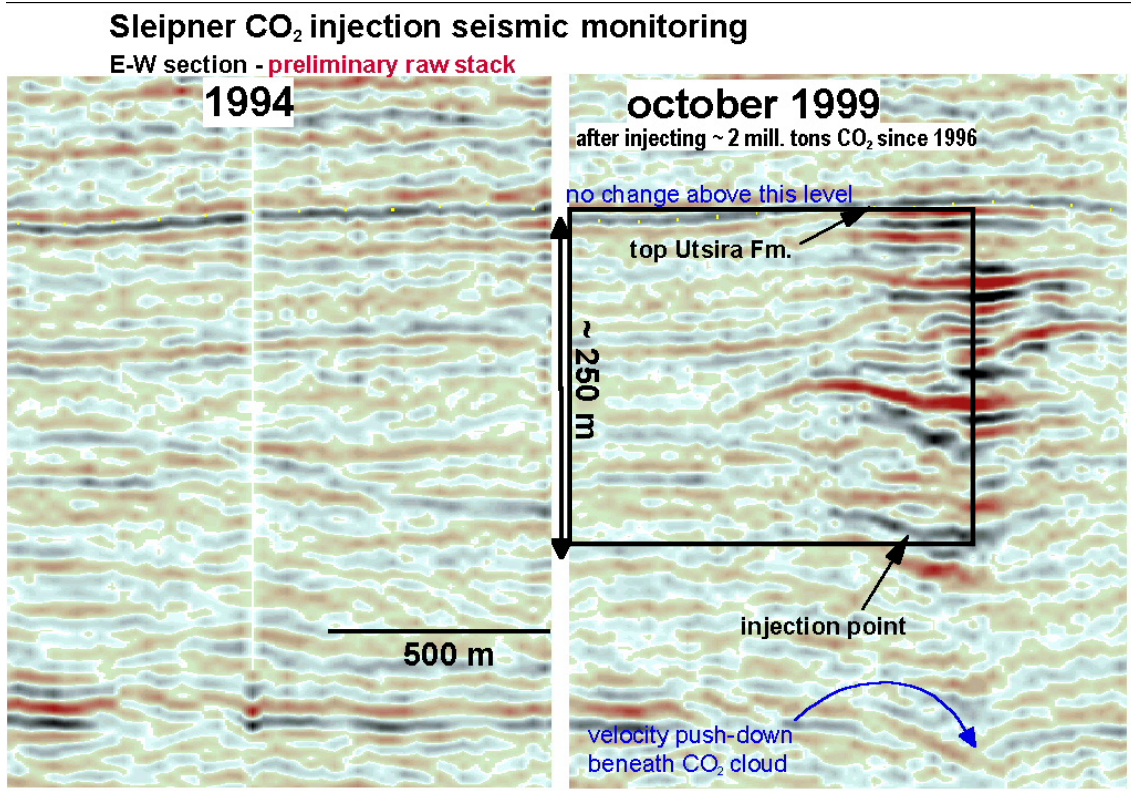


Figure 4.7 Seismic lines from utsira formation. First data set as supplied from Statoil. The black rectangle drawn on the right seismic profile corresponds approximately to the mirror image of simulated saturation profile in Figure 4.6.

A brief update of the reservoir model, based on the interpretations above was implemented, and the result is shown in Figure 4.8.

4.5 Sensitivity with respect to permeability.

The difference in permeability that has been measured at two laboratories was surprisingly large, 3.3 Darcy vs. 0.700 Darcy. The variation in saturation due to varying permeability was therefore studied. In a simulation the permeability was reduced with a factor of ten and set to 0.33 Darcy compared to 3.3 Darcy which is the default permeability that was used in all previous simulations. The result is shown in Figure 4.9.

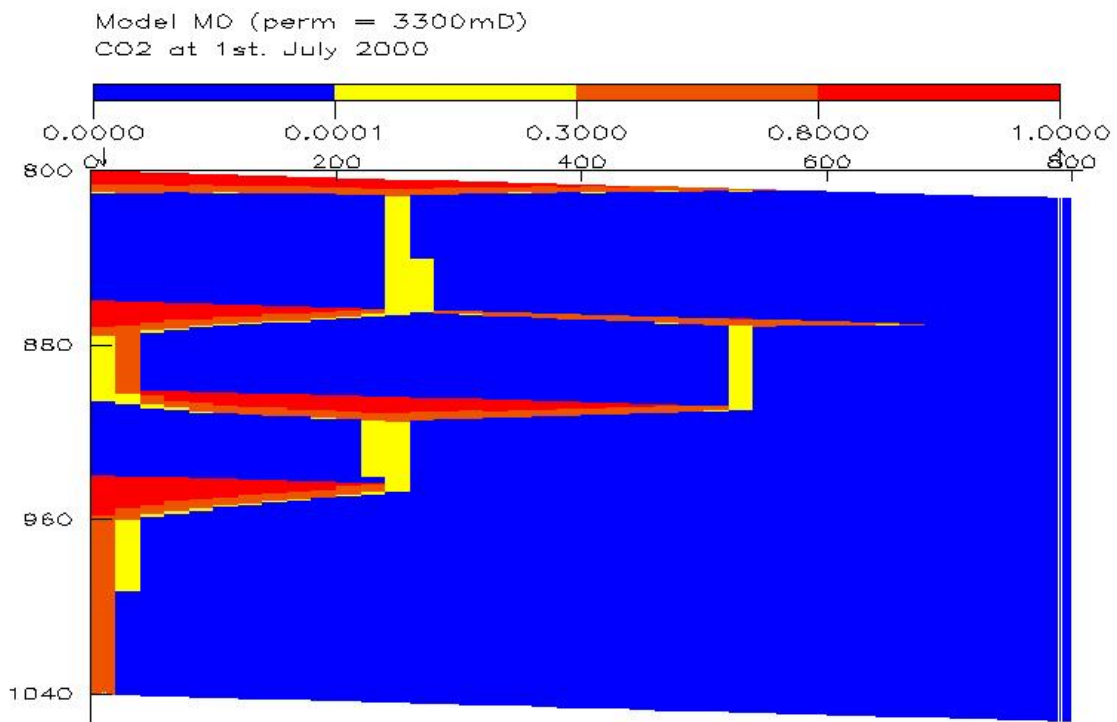


Figure 4.8 Simulated saturation profile of the updated reservoir model. Overall permeability is 3.3 Darcy

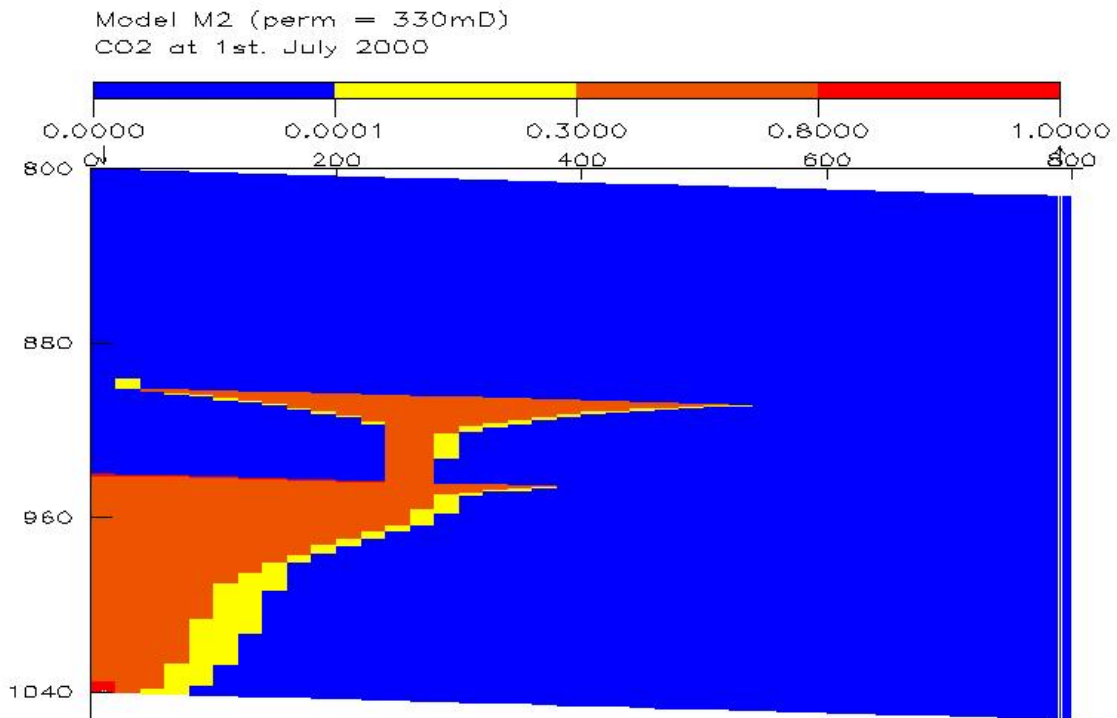


Figure 4.9 Simulated saturation profile of the updated reservoir model. Overall permeability is 0.33 Darcy

The CO₂ is migrating much slower to the seal, but the pattern is recognised from the previous case

In the next simulation a vertical permeability contrast is created and in the left half of the reservoir the permeability is set 3.3 Darcy and in the right half the permeability is set to 0.33 Darcy. The result is shown in Figure 4.10. The difference in distribution is not significant despite the permeability contrast.

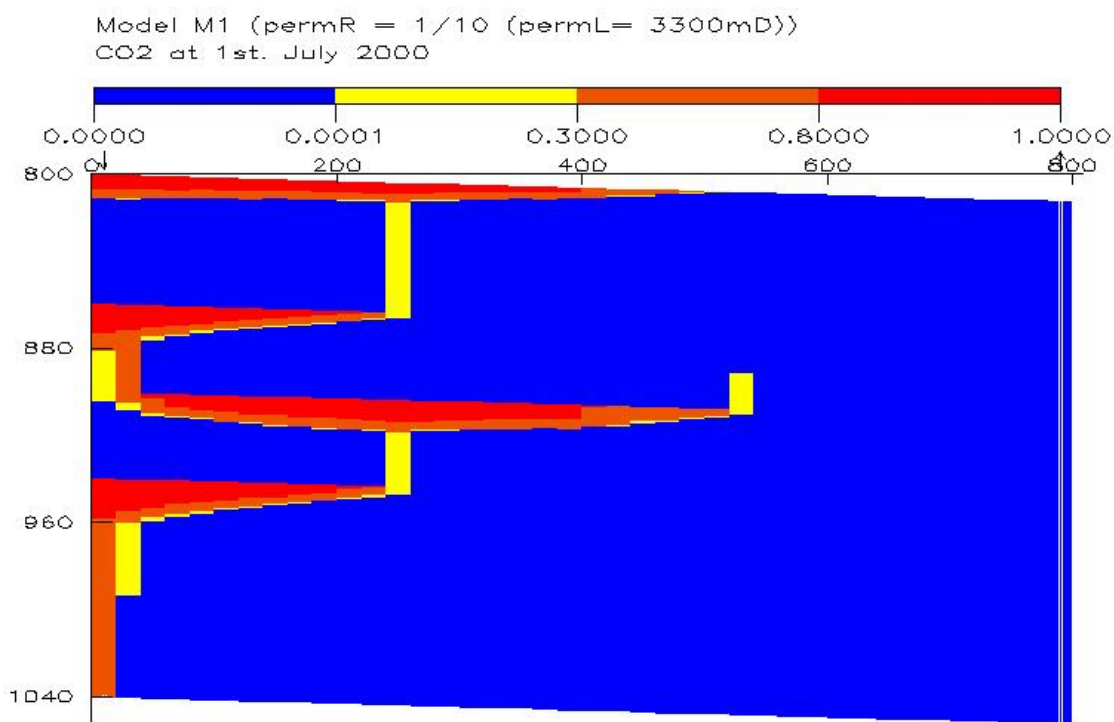


Figure 4.10 Simulated saturation profile of the updated reservoir model. The left half is 3.3 Darcy while the right half is 0.33 Darcy

4.6 Discussion of reservoir simulation

The most important parameter for the reservoir simulations is to model the horizontal heterogeneities in form of impermeable shales. Other heterogeneities seem to have less importance. The large uncertainties in these simulations must be emphasised, especially due to the lack of information of transport properties in the entire vertical column. The models (homogeneous and heterogeneous) were chosen to represent extremes with respect to CO₂ migration. Other extreme heterogeneities could, however, be envisaged that will result in smaller CO₂ accumulations. One such case is that there exists a deep semi-permeable shale that will trap large amount of CO₂, but at the same time allow CO₂ to migrate through the whole shale area. Large water volumes will in this case be contacted by CO₂ resulting in much larger fraction of CO₂ dissolved as shown by Lindeberg (1996).

In the cases where CO₂ solubility is included only 5 to 12% of the injected CO₂ will be dissolved at December 1st. 1998. Since no up-scaling of the solubility has been implemented, it is assumed that these figures are too large.

5. Rayleigh convection

5.1 Summary

A 2D formulation for deposition of CO₂ in underground aquifer is given. CO₂ is soluble in water and increases the density of the liquid phase. The formulation given accounts for diffusion and convective flow. A steady state background temperature is also included in the model, and a linearized equation of state (EOS) is applied. The two primary variables solved for are the pressure, p , and the CO₂ concentration c_1 . The presentation is organised as follows: First the pressure and concentration equations are derived. These equations are then written on dimensionless form and the pressure is expressed using the scaled “dynamic pressure”. The equations are then simplified using a (non-singular) perturbation analysis related to the relevant physical regime. The equations have been discretised using a fully implicit finite difference formulation, and the code is currently being tested.

5.2 Defining equations

Let the reservoir have length L and height H . A positive oriented (x, z) co-ordinate system is employed, and the reservoir is assumed to have no dip. Darcy’s law for the volumetric flux is

$$\vec{J}_v = -\frac{k}{\nu}(\vec{\nabla}p + \rho g \vec{\nabla}z). \quad (5.1)$$

Here $k(x, z) = \begin{bmatrix} k_x & 0 \\ 0 & k_z \end{bmatrix}$ is the (non-constant) permeability matrix, ν the constant fluid viscosity, p the pressure, ρ the fluid density, and g the acceleration of gravity.

The gradient of the chemical potential of component i , $i = 1, 2$, where $i = 1$ is CO₂, and $i = 2$ is H₂O, is given by

$$\vec{\nabla}\mu_i = \frac{RT}{c_i} \vec{\nabla}c_i + \frac{\vec{\nabla}p}{C} + M_i g \vec{\nabla}z. \quad (5.2)$$

Here R is the universal gas constant, T the temperature, c_i the molar concentration of component i , C the total molar concentration, and M_i is the mass per mole of component i . In this study (*i.e.* physical regime) it is permissible to neglect the two last terms of (5.2) (REF), and only the first term in (5.2) will be used in the analysis below.

The molar flux of each component is given by combining diffusion and convection

$$\vec{J}_i = L_i \frac{1}{T} \vec{\nabla} \mu_i + c_i \vec{J}_v. \quad (5.3)$$

Assuming an ideal solution, one has

$$L_i = -D \frac{c_i}{R}, \quad i = 1, 2. \quad (5.4)$$

Here $D(x, z) = \begin{bmatrix} D_x & 0 \\ 0 & D_z \end{bmatrix}$ is the (macroscopic) diffusivity, which can be anisotropic and non-constant in the formulation given below.

A lateral constant steady state temperature field is assumed:

$$T(z) = T_0 + \frac{T_1 - T_0}{H} (H - z). \quad (5.5)$$

Remark:

The characteristic time scale for thermal conduction is $t_{therm} = \frac{H^2}{D_{therm}}$. The

characteristic time scale for molecular diffusion of CO₂ is $t_{diff} = \frac{H^2}{D^*}$,

while one has (as will be seen in section 5.4) $t_{conv} = \frac{H \nu \varphi^*}{k_z^* g \Delta \rho_c}$ as characteristic time scale

for (density driven) convective flow. The following applies in the physical regime considered here

$$t_{conv} \ll t_{therm} \ll t_{diff}.$$

For the parameters listed in section 5.6 one has

$$t_{conv} = 14 \text{ years}, \quad t_{therm} = 3500 \text{ years}, \quad t_{diff} = 140\,000 \text{ years},$$

As it is the very slow diffusion process that triggers the fast convection process, the assumption of a steady state background temperature is appropriate, at least at times before a significant amount CO₂ has diffused into the water phase. However, when convective flow dominates on the short time scale (after a significant amount of CO₂ has dissolved into the water), convective transport of thermal energy can be important to include in the model. Note that t_{conv} would be comparable to t_{diff} if one had a low permeable reservoir with permeability of magnitude 0.1 mD .

The equation of state (EOS) is given by

$$C(p, c_1, T(z)) = C_0 \left(1 + E_p (p - p_0) + E_c c_1 - E_T (T(z) - T_0) \right), \quad (5.6)$$

where p_0 is the initial pressure and T_0 the temperature at the top of the reservoir. E_p, E_c, E_T are three constants defining the EOS.

The liquid molar density satisfies

$$C = c_1 + c_2. \quad (5.7)$$

Thus using (5.6) the liquid density is given by

$$\rho(p, c_1, z) = M_1 c_1 + M_2 c_2 = C_0 M_2 \left(1 + \frac{M_1 - M_2}{M_2} \left[\frac{1}{C_0} + E_c \right] c_1 + E_p (p - p_0) - E_T (T_1 - T_0) \frac{H - z}{H} \right). \quad (5.8)$$

Let $\varphi = \varphi(x, z)$ be the porosity. Then mass conservation for component i reads

$$\varphi \frac{\partial c_i}{\partial t} + \nabla \cdot \vec{J}_i = 0, \quad i = 1, 2. \quad (5.9)$$

Equations (5.1)-(5.9) will define the equations for the primary (*i.e.* unknown) variables p and c_1 . In addition, initial conditions and boundary conditions have to be specified.

The *initial condition* is $c_1 = 0$ and $\vec{J}_v = 0$ (*i.e.* no CO₂ dissolved, and hydrostatic equilibrium).

The *boundary conditions* are implemented by setting $k_z = 0$ for $z = 0$ and $z = H$, and $k_x = 0$ for $x = 0$ and $x = L$. Thus there is no convective flow across the boundary of the reservoir. The diffusion coefficient is set to $D_x = 0$ for $x = 0$ and $x = L$, $D_z = 0$ for $z = 0$. Diffusion of component 1 from above into the reservoir is achieved by setting $c_1 = c_{top}(x)$ with non-zero diffusivity D_z for $z = H$.

5.3 Derivation of pressure and concentration equation

The pressure equation is derived as follows:

Adding the two expressions in (5.9), and using (5.7) gives

$$\varphi \frac{\partial C}{\partial t} + \nabla \cdot (\vec{J}_1 + \vec{J}_2) = 0$$

Thus (5.6) gives

$$\varphi \left(C_0 E_p \frac{\partial p}{\partial t} + C_0 E_c \frac{\partial c_1}{\partial t} \right) + \bar{\nabla} \cdot \bar{J}_T = 0 .$$

One sees that subtracting $C_0 E_c$ times the concentration equation of component 1 from this equation gives

$$\begin{aligned} \varphi \left(C_0 E_p \frac{\partial p}{\partial t} \right) + \bar{\nabla} \cdot (\bar{J}_T - C_0 E_c \bar{J}_1) &= 0 \Leftrightarrow \\ (C_0 E_p) \varphi \frac{\partial p}{\partial t} + \bar{\nabla} \cdot \bar{J}_p &= 0 \end{aligned} \quad (5.10)$$

where

$$\bar{J}_p = \bar{J}_T - C_0 E_c \bar{J}_1 .$$

(5.10) is the *pressure* equation.

The *concentration* equation is the mass (or molar) conservation equation for component 1:

$$\varphi \frac{\partial c_1}{\partial t} + \bar{\nabla} \cdot \bar{J}_1 = 0 . \quad (5.11)$$

5.3.1 Derivation of \bar{J}_p

Recall that the two last terms in (5.2) are disregarded. Then the molar flux of component i , $i = 1, 2$, is

$$\bar{J}_i = -D \bar{\nabla} c_i - \frac{c_i}{\nu} k [\bar{\nabla} p + \rho g \bar{\nabla} z] . \quad (5.12)$$

Using (5.7), the total molar flux $\bar{J}_1 + \bar{J}_2$ is

$$\bar{J}_T = -D \bar{\nabla} C - \frac{C}{\nu} k [\bar{\nabla} p + \rho g \bar{\nabla} z] .$$

Thus

$$\bar{J}_p = \bar{J}_T - E_c C_0 \bar{J}_1 =$$

$$-D \bar{\nabla} C - \frac{C}{\nu} k [\bar{\nabla} p + \rho g \bar{\nabla} z] - E_c C_0 \left\{ -D \bar{\nabla} c_1 - \frac{C_1}{\nu} k [\bar{\nabla} p + \rho g \bar{\nabla} z] \right\} ,$$

giving

$$\vec{J}_p = -D\vec{\nabla}\tilde{C} - \frac{\tilde{C}}{\nu}k[\vec{\nabla}p + \rho g\vec{\nabla}z], \quad (5.13)$$

where

$$\tilde{C} = \tilde{C}(p, z) = C_0 \left(1 + E_p(p - p_0) - E_T(T_1 - T_0) \frac{H - z}{H} \right).$$

5.4 Scaling of equations

The equations are now written on dimensionless form. The reservoir is initially in hydrostatic equilibrium with no CO₂ dissolved in the water. Then the CO₂ diffuses into the reservoir from the top increasing the density of the water phase at the top of the reservoir. For lateral homogenous conditions this is a physical system in an unstable equilibrium state. Any lateral non-homogeneity (in permeability, diffusivity, or boundary values of CO₂ density) would then trigger instability initiating convective flow due to density differences. The characteristic time scale for the diffusion process and the time scale for convection may differ significantly. Thus in general there are two characteristic time scales in the model considered. Below we scale time using the time scale characteristic to the convective flow. It will be seen that the characteristic time scale for the diffusion process is much longer, unless the permeability is very small.

The equations are formulated in terms of the dynamic pressure, and scaled relative to the hydrostatic pressure increase experienced at the bottom when going from no CO₂ to a reservoir saturated with CO₂. From (5.8) one sees that the corresponding density increase is

$$\Delta\rho_c = C_0 M_2 \left[\frac{M_1 - M_2}{M_2} \frac{1}{C_0} + E_c \right] c^*,$$

where c^* is the maximal molar concentration of CO₂.

Let $\rho_0 = M_2 C_0$, and let φ^* , k_x^* , k_z^* , D_x^* , D_z^* be the typical, or average, values for porosity, permeability, and diffusivity respectively. The following scaling is applied

$$t \rightarrow \frac{H\nu\varphi^*}{k_z^*g\Delta\rho_c} t, \quad x \rightarrow Lx, \quad z \rightarrow Hz,$$

$$c_1 \rightarrow c^*c_1, \quad \tilde{C} \rightarrow C_0\tilde{C}, \quad T \rightarrow T_0T, \quad \rho \rightarrow \rho_0\rho,$$

$$p \rightarrow p_0 + \rho_0gH(1 - z) + \Delta\rho_cgHp, \quad (z \text{ is scaled})$$

$$\varphi \rightarrow \varphi^*\varphi, \quad k_x \rightarrow k_x^*k_x, \quad k_z \rightarrow k_z^*k_z, \quad D_x \rightarrow D_x^*D_x, \quad D_z \rightarrow D_z^*D_z$$

Note that the scaled variables are of magnitude 1, or varies typically from 0 to 1.

5.4.1 Scaled constitutive relations

The scaled expressions for \tilde{C} and ρ are derived. In scaled variables one has

$$\tilde{C} = 1 + (E_p \Delta \rho_c g H) p + (E_p \rho_0 g H - E_T (T_1 - T_0))(1 - z)$$

Let

$$a_p = E_p \Delta \rho_c g H \text{ and}$$

$$a_z = E_p \rho_0 g H - E_T (T_1 - T_0).$$

Then

$$\tilde{C} = 1 + a_p p + a_z (1 - z), \quad (5.14)$$

and

$$\frac{\partial \tilde{C}}{\partial x} = a_p \frac{\partial p}{\partial x}, \quad \frac{\partial \tilde{C}}{\partial z} = a_p \frac{\partial p}{\partial z} + a_z \quad (5.15)$$

where the derivative is taken with respect to scaled x and z .

Furthermore, from (5.8) one derives

$$\rho = \frac{\Delta \rho_c}{\rho_0} c_1 + \tilde{C}$$

for the scaled density.

5.4.2 Scaled concentration equation

The concentration equation in unscaled variables is

$$\varphi \frac{\partial c_1}{\partial t} + \frac{\partial}{\partial x} J_{1x} + \frac{\partial}{\partial z} J_{1z} = 0,$$

where

$$\vec{J}_p = [J_{1x}, J_{1z}].$$

Expressed in dimensionless variables the concentration equation reads

$$\varphi^* \varphi \frac{\partial (c^* c_1)}{\frac{H \nu \varphi^*}{k_z^* g \Delta \rho_c} \partial t} + \frac{1}{L} \frac{\partial}{\partial x} \left(-D_x^* D_x \frac{1}{L} \frac{\partial}{\partial x} (c^* c_1) - (c^* c_1) \frac{k_x^* k_x}{\nu} \left(\frac{1}{L} \frac{\partial}{\partial x} (\Delta \rho_c g H p) \right) \right) +$$

$$\frac{1}{H} \frac{\partial}{\partial z} \left(-D_z^* D_z \frac{1}{H} \frac{\partial}{\partial z} (c^* c_1) - (c^* c_1) \frac{k_x^* k_x}{\nu} \left(\frac{1}{H} \frac{\partial}{\partial z} (\Delta \rho_c g H p + \rho_0 g H (1-z)) + \rho_0 \rho g \right) \right) = 0$$

\Leftrightarrow

$$\varphi \frac{\partial c_1}{\partial t} - \left(\frac{H^2 k_x^*}{L^2 k_z^*} \right) \frac{\partial}{\partial x} \left(\left(\frac{D_x^* \nu}{H k_x^* g \Delta \rho_c} \right) D_x \frac{\partial c_1}{\partial z} + c_1 k_x \frac{\partial p}{\partial z} \right) - \frac{\partial}{\partial z} \left(\left(\frac{D_x^* \nu}{H k_x^* g \Delta \rho_c} \right) D_z \frac{\partial c_1}{\partial z} + c_1 k_z \left(\frac{\partial p}{\partial z} + \frac{\rho_0}{\Delta \rho_c} (\rho - 1) \right) \right) = 0$$

giving

$$\varphi \frac{\partial c_1}{\partial t} - R \frac{\partial}{\partial x} \left(\tau_x D_x \frac{\partial c_1}{\partial x} + c_1 k_x \frac{\partial p}{\partial x} \right) - \frac{\partial}{\partial z} \left(\tau_z D_z \frac{\partial c_1}{\partial z} + c_1 k_z \left(\frac{\partial p}{\partial z} + c_1 + e_p p + e_z (1-z) \right) \right) = 0 \quad (5.16)$$

with

$$R = \frac{H^2 k_x^*}{L^2 k_z^*}, \quad \tau_x = \frac{D_x^* \nu}{H k_x^* g \Delta \rho_c}, \quad \tau_z = \frac{D_z^* \nu}{H k_z^* g \Delta \rho_c},$$

$$e_p = E_p \rho_0 g H, \quad e_z = \frac{\rho_0}{\Delta \rho_c} (e_p - E_T (T_1 - T_0))$$

as dimensionless groups. In the scaled pressure equation one additional dimensionless number enters ,

$$a_p = E_p \Delta \rho_c g H = e_p \frac{\Delta \rho_c}{\rho_0}.$$

Thus, the physics of this problem (i.e. the physical regime consistent with the perturbation analysis in section 2.4) is governed by the above six independent dimensionless numbers. R is usually referred to as the aspect ratio, and can be interpreted as the ratio of the two time scales t_z and t_x related to applying the same (viscous) potential drop in the vertical and horizontal direction respectively. The numbers τ_x and τ_z are the Peclét numbers, defining the relative importance of diffusion to (the density driven) convective flow. These two numbers represent the ratio of convection and diffusion time scales. e_p and e_z define the importance of the dynamic pressure (i.e. the derivation from hydrostatic equilibrium) and depth respectively relative to c_1 -concentration in the expression for phase density. a_p is the ratio between the time scale for propagation of convective flow of CO₂ concentration and the time scale of propagation of pressure perturbations.

5.4.3 Scaled pressure equation

The pressure equation in unscaled variables is given by (5.10):

$$(E_p C_0) \varphi \frac{\partial p}{\partial t} + \frac{\partial}{\partial x} J_{px} + \frac{\partial}{\partial z} J_{pz} = 0.$$

In scaled variables one obtains

$$(E_p C_0) \varphi^* \varphi \frac{1}{H \nu \varphi^*} \frac{\Delta \rho_c g H \partial p}{\partial t} + \frac{1}{L} \frac{\partial}{\partial x} \left(-D_x^* D_x \frac{1}{L} \frac{\partial (C_0 \tilde{C})}{\partial x} - \frac{C_0 \tilde{C} k_x^* k_x}{\nu} \frac{1}{L} \frac{\partial (\Delta \rho_c g H p)}{\partial x} \right) +$$

$$\frac{1}{H} \frac{\partial}{\partial z} \left(-D_z^* D_z \frac{1}{H} \frac{\partial (C_0 \tilde{C})}{\partial z} - \frac{C_0 \tilde{C} k_z^* k_z}{\nu} \left(\frac{1}{H} \frac{\partial (\Delta \rho_c g H p + \rho_0 g H (1-z))}{\partial z} + \rho_0 \rho g H \frac{1}{H} \right) \right) = 0$$

giving

$$a_p \varphi \frac{\partial p}{\partial t} - R \frac{\partial}{\partial x} \left(\tau_x D_x \frac{\partial \tilde{C}}{\partial x} + \tilde{C} k_x \frac{\partial p}{\partial x} \right) - \frac{\partial}{\partial z} \left(\tau_z D_z \frac{\partial \tilde{C}}{\partial z} + \tilde{C} k_z \left(\frac{\partial p}{\partial z} + \frac{\rho_0}{\Delta \rho_c} (\rho - 1) \right) \right) = 0.$$

Then, using (5.14) and the expression for ρ , one obtains

$$a_p \varphi \frac{\partial p}{\partial t} - R \frac{\partial}{\partial x} \left((\tau_x a_p D_x + \tilde{C} k_x) \frac{\partial p}{\partial x} \right) -$$

$$\frac{\partial}{\partial z} \left((a_p \tau_z D_z + \tilde{C} k_z) \frac{\partial p}{\partial z} + a_z \tau_z D_z + \tilde{C} k_z (c_1 + e_p p + e_z (1-z)) \right) = 0. \quad (5.17)$$

5.5 Perturbation analysis

The concentration equation (5.16) is kept without disregarding any terms (except the two last terms in (5.2) disregarded initially). The pressure equation, however, is simplified as follows:

In (5.17), for the coefficient of $\frac{\partial p}{\partial x}$ one has

$$\tau_x a_p D_x + \tilde{C} k_x = \tau_x a_p D_x + k_x (1 + a_p p + a_z (1-z))$$

$\tau_x a_p, a_p, a_z \ll 1$, giving

$$\tau_x a_p D_x + \tilde{C} k_x \approx k_x.$$

Similarly, for the coefficient of $\frac{\partial p}{\partial z}$, one has $a_p \tau_z \ll 1$

giving

$$\tau_z a_p D_z + \tilde{C} k_z \approx k_z.$$

Furthermore,

$a_z \tau_z \ll e_p$ and $a_z \tau_z \ll e_z$, and by putting $\tilde{C} \approx 1$, the pressure equation simplifies to

$$a_p \varphi \frac{\partial p}{\partial t} - R \frac{\partial}{\partial x} \left(k_x \frac{\partial p}{\partial x} \right) - \frac{\partial}{\partial z} \left(k_z \left(\frac{\partial p}{\partial x} + c_1 + e_p p + e_z (1 - z) \right) \right) = 0. \quad (5.18)$$

(5.18) is linear, but is coupled to the non-linear concentration equation (5.16).

5.6 Validation of perturbation analysis

Typical values for deposition of CO₂ in a high permeable aquifer is as follows:

$$M_1 = 44 \cdot 10^{-3} \text{ kg mol}^{-1} \quad (\text{CO}_2)$$

$$M_2 = 18 \cdot 10^{-3} \text{ kg mol}^{-1} \quad (\text{H}_2\text{O})$$

$$\nu = 1.0 \cdot 10^{-3} \text{ kg m}^{-1} \text{ s}^{-1}$$

$$\varphi^* = 0.3$$

$$T_0 = 310 \text{ K}$$

$$T_1 = 318 \text{ K}$$

$$D^* = 3 \cdot 10^{-9} \text{ m}^2 \text{ s}^{-1}$$

$$k^* = 10^{-12} \text{ m}^2$$

$$R = 8.3 \text{ kg m}^2 \text{ s}^{-2} \text{ K}^{-1} \text{ mol}^{-1}$$

$$L = 2000 \text{ m}$$

$$H = 200 \text{ m}$$

$$E_p = 4.1 \cdot 10^{-5} \text{ bar}^{-1}$$

$$E_c = -1.6 \cdot 10^{-5} \text{ mol}^{-1} \text{ m}^3$$

$$E_T = 3.1 \cdot 10^{-4} \text{ K}^{-1}$$

$$c^* = 1.4 \cdot 10^3 \text{ mol m}^{-3}$$

$$C_0 = 5.6 \cdot 10^4 \text{ mol m}^{-3}$$

$$D_{therm} = 3.7 \cdot 10^{-7} \text{ m s}^{-2}$$

Thus, approximately,

$$\begin{aligned}R &= 10^{-2}, \\ \tau_x = \tau_z &= 10^{-4}, \\ e_p &= 10^{-2}, \\ e_z &= 5 \cdot 10^{-1}, \\ a_p &= 10^{-4}, \\ a_z &= 5 \cdot 10^{-3}.\end{aligned}$$

The perturbation analysis is justified as all neglected terms in section 5.6 are more than two orders of magnitude less than 1.

6. References

- Altunin, V.V., Gadetskii, 1971: (title translated to English:) "Equation of State and Thermophysical properties of Liquid and. Gaseous Carbon Dioxide", *Teploenergetica*, 18, (3), 81-84
- Angus, S., Armstrong, B., de Reuck, K.M. (editors.) "International Thermodynamic Tables of the Fluid State, 1973: Carbon Dioxide", International Union of Pure and Applied Chemistry, Project Centre. London, UK
- Arai, Y., Kamanishi, G.I., Saiyo, S., 1971: "The experimental determination of the P-V-T-X relations for the Carbon dioxide-nitrogen and the carbon dioxide-methane systems", *J-Chem. Eng. Japan* 4, p113 – 122
- Duan, Z., Møller, N., Weare, J.H., 1992: "An equation of the for the CH₄-CO₂-H₂O system: II. Mixtures from 50 to 1000°C and 0 to 1000 bar, *Geochimica et Cosmochimica Acta*, Vol 56, p2605-2617.
- Eggen, 1984: "Modelling of subsidence, hydrocarbon generation and heat transport in the Norwegian North Sea", IFP
- Eggers, R., Jäger, Ph.T. 1994: "Die Einfluss vom Grenzflächenerscheinungen auf den Stoffübergang und die Prozessführung in Gegenstromkolonnen mit überkritischem CO₂", *Wärme und Stoffübertragung*, 29, p 373- 377.
- Encyclopedie Des Gaz, L' AIR LIQUIDE, p 333 – 368.
- Engineering Science Data, 1968: "Density of Water Substance", Institute of Mechanical Engineers , London.
- Enick, R.M. and Klara, S.M., 1990: "CO₂ Solubility in Water and Brine Under Reservoir Conditions", *Chem. Eng. Comm.*, Vol. 90, pp. 23-33.
- Golubev, I.F., 1969: "Viscosity if gases and gasmixtures, *Fizmatgiz*, 1950, Reproduced by Vukalovich, M.P., Altunin, V.V., "Thermophysical Properties of Carbon Dioxide", Collet's Publishers LTD. London & Wellingborough p 387
- Holloway, S., Bateman, K., Barbier, J., Doherty, P., Fabriol, H., Harrison, R., Heederik, J.P., van der Meer, L.G.H., Czernichowski-Lauriol, I., Lindeberg, E.G.B, Pearce, J.M., Summerfield, I.R., Rochelle, C., Sanjuan, B., Schartzkopf, T., Kaarstad, O., Berger, B. 1996: "The Underground Disposal of Carbon Dioxide", Final Report of JOULE II Project no. CT92-0031, Non Nuclear Energy R&D Programme

- Holt, T., Jensen, J-I., Lindeberg, E.G.B., 1995: "Underground Storage of CO₂ in Aquifers and Oil Reservoirs", Energy Convers. Mgmt Vol 36, No 6-9 pp 535-538
- Hough, E.W., Heuer, G.J., Walker, J.W. 1959, "An improved pendant Drop, Interfacial tension Apparatus and data for Carbon Dioxide and water", Petroleum Transaction, vol 216, p 469
- Kennedy, G.C., 1954, "Pressure-volume-temperature relations in CO₂ at elevated temperature and pressures", Amer. J. Sci., 252, p225 – 241.
- Korbøll, R., Kaddour, A., 1995: "Sleipner vest CO₂ disposal- injection of removed CO₂ into the Utsira formation". Energy Convers. Mgmt. Vol. 36 No 6 - 9., page 509-512,.
- Krillin, K.A., Ulybin, S.A., Zherdev, E.P. 1969, "CO₂ density on 35, 30, 20 and 10°C isotherms at pressures up to 500 bar", Therm. Eng. 16, p137 – 139
- Lindeberg, E.G.B, 1996 "Escape of CO₂ from Aquifers". Energy Convers. Mgmt. Vol. 38 Suppl., page s229-s234
- Michels, A., Michels, C., 1935, "Isotherms of CO₂ between 0° and 150° and pressures form 16 to 250 atm (Amagat densities 16-206)", Proc. Roy. Soc. A153, 201.214
- Numere, D., Brigham, W.E., Standing, M.B. 1977, "Correlations for Physical Properties of petroleum reservoir Brines", Petroleum Research Institute, Stanford University, November 1977, p 8
- Reamer, H.H., Olds, R.H., Sage, B.H., Lacey, W.N., 1944: "Phase Equilibria in Hydrocarbon Systems: Methane-Carbondioxide System in the Gaseous Region", Ind. Eng. Chem. 36, p88 – 90.
- Renner, T.A., 1988: "Measurement and Correlation of Diffusion at Reservoir Conditions for CO₂ and Rich-Gas Applications", SPE reservoir Engineering, May, p 517 – 23
- van der Sluijs, J., 1991: "Interactive thermodynamic data generator. Based on the Energpack routines by Evert Nieuwlaar", Department of Science Technology and Society, University of Utrecht (RUU), the Netherlands
- Vukalovich M.P., Kobelev V.P., Timoshenko N.I., 1998: "Experimental investigation of CO₂ density at temperatures from 0 to 35°C and pressure up to 300 bar", Therm. Eng. 15, 103 – 106
- Vukalovich, M.P., Altunin, V.V., 1969: "Thermophysical Properties of Carbon Dioxide", Collet's Publishers LTD. London & Wellingborough p 419